Chapter 5

An interplay between ferromagnetic and magnetic glassy state in Fe doped $(SnTe)_{1-x}Sb_x$ bulk alloys

5.1 Introduction

Transition metal doped tin chalcogenide compound semiconductors belonging to IV – VI group are the extensively studied systems of dilute magnetic semiconductors. Due to their narrow band gap, they are found to be good candidates for thermoelectric, photovoltaic and optical applications [1-3]. One such compound semiconductor is Tin Telluride (SnTe) which has a narrow band gap of 0.18 eV [4]. SnTe can exist in three distinct crystal structures at different range of temperatures. They have a cubic rock salt crystal structure having space group F*m*-3*m* at room temperature. However, at temperatures below 100 K, SnTe undergoes a ferroelectric/displacive transition accompanied by a change in its crystal structure from cubic to rhombohedral of space group R3*m* [5]. It is also found to exist in orthorhombic structure at high pressure having Pnma space group [6]. Stoichiometric SnTe compound has ionic nature whereas off stoichiometry SnTe alloy possesses metallic behaviour [7]. Along with Sn^{2+} vacancies that are created by excess solubility of Te in SnTe, generation of holes are also responsible for this metallic nature. Therefore, excess of Te in SnTe alloy makes it a p-type semiconductor. On the other hand, off stoichiometric SnTe alloy that consists of excess Sn having form Sn_xTe_{1-x} (where $0.5<x<1$) give rise to two-phases, that of Sn and SnTe. This gives it an n-type semiconductor feature [8]. SnTe is also identified as a topological crystalline insulator whose topological behaviour results from its non-magnetic nature [9, 10].

There is an increase in the band gap of SnTe at higher temperatures because of a reduction in valence band dispersion caused by a decrease in the orbital overlap interaction as a result of an increase in bond length brought on by thermal expansion [11]. The increase in band gap can contribute to improved thermoelectric properties as well as can enhance properties of the system to develop optoelectric devices. Widening of band gap is also desirable in dilute magnetic semiconductors for they present room temperature ferromagnetism [12]. Indium doped SnTe nanowires showed enhanced thermoelectric performance with peak figure of merit (zT) value around 1.1 at about 873K [13]. Bulk SnTe co-doped with Ca and In has shown further increase in the zT value to about 1.65 at 840K [14]. Indium and Mn co-doped bulk SnTe alloys show peculiar feature wherein the band gap values were found to be decreasing and then increasing with doping [15]. At the same time, Raman peaks in In and Mn co-doped bulk SnTe alloys were found to shift to lower wavenumbers which is due to changes in the force constant. Similar effects are seen in the Raman peaks of Sb-doped SnTe single crystals [16]. Raman peaks of Eu-doped SnTe QDs also show shifting as a result of stress caused due to doping [17]. Also, presence of ferroelasticity in Cr-doped SnTe single crystals below phase transition point at about 100 K was realized, implying that below a critical temperature, a spontaneous strain arises in the system [18]. Substituting In at the Sn site of topological crystalline insulator SnTe crystals resulted in superconducting behaviour that could be a good candidate for 3D topological crystalline superconductivity [19]. Similarly, in Ag doped SnTe polycrystalline samples $Sn_{1-x}Ag_xTe$ where the ideal quantity of Ag is x = 0.2, bulk superconductivity with a Curie temperature of 2.4 K was observed for x = 0.15 – 0.25 [20].

The theoretical and experimental studies carried out to explore magnetic properties of SnTe has doping of transition metals like Mn, V, Cr, Co and Ni into it. Mn-doped SnTe thin films have possible ferromagnetic or antiferromagnetic order or even existence of spin glass state [21-24]. Studies on the $Sn_{1-x}Cr_xTe$ DMS system for low concentrations of Cr from x = 0.004 to 0.012 demonstrated a spin-glass-like state as a result of short-range direct magnetic interactions present in

Cr-rich clusters [25]. However, another study on $Sn_{1-x}Cr_xTe$ crystals for higher concentration of Cr of x > 0.2 at. % exhibited ferromagnetism whereas below this concentration, substantial diamagnetic behaviour is seen due to the diamagnetic background of SnTe crystal [26]. Among all the 3d-transition-metal-doping in SnTe, Mn was found to have largest magnetic moment and its effective hybridization with valence state allows for the development of ferromagnetic order [27]. In $Sn_{1-x}Fe_xTe$ crystal, ferromagnetism was also seen for x = 0.01, up to 500°C [28].

In the present chapter, SnTe is doped with dilute amount of transition element Fe (0.05) and in addition, it is also substituted with donor impurity (Sb) to prepare the bulk alloys having form $Fe_{0.05}(SnTe)_{1-x}Sb_x$. Charge carrier induced effect is investigated in their properties by adopting different characterization techniques as discussed in the subsequent sections.

5.2 Experimental Procedure

$Fe_{0.05}(SnTe)_{1-x}Sb_x$ powder samples (x = 0, 0.01, 0.03 and 0.05) were prepared by modified solid state reaction technique. Accurate weight measurements were taken for the requisite ratios of SnTe, Sb and Fe (Alfa Aesar, 99.999% pure) that are commercially available and they were ground using an Agate mortar and pestle thoroughly to get fine powder. These powder samples were then loaded in quartz tube ampoules which were closed at one end. The ampoules were evacuated at a pressure > 10^{-5} Torr using a rotary pump and then sealed. Using oxy-butane flame, the sealed ampoules were heated repeatedly to reach desired temperatures so that the powders liquefy. Finally, after a homogeneity was reached, the ampoules were quenched in ice cold water in order to solidify the sample. The obtained ingots were crushed and grounded for homogenous mixing to obtain fine powders that were then characterized for their properties.

5.2.1. Characterization Techniques

Structural aspects of the samples were studied using Bruker D8 Advance X-ray Diffractometer (XRD) having CuK$_\alpha$ radiation of wavelength 1.5406 Å in the range of 20° to 70°. The topographical images of the samples were analyzed using Hitachi model S 3400 N Field Emission Scanning Electron Microscope (FESEM). Using Fourier Transform Infrared Spectroscopy (Shimazdu FTIR – 8400 S), band gap values were calculated. Using Quantum Design's Physical Property Measurement System (PPMS), measurements of temperature and magnetic field dependent electrical resistivity and magnetic resistivity were made. Magnetic measurements including DC and AC were carried our using Quantum design make Superconducting Quantum Interface Device – Vibrating Sample Magnetometer (SQUID-VSM) magnetometer equipped with Pulse Tube Cooler in the temperature range 10 K – 300 K and magnetic field range of up to 7T.

5.3 Results and Discussion

5.3.1 Structural Studies

X-ray diffraction patterns of $Fe_{0.05}(SnTe)_{1-x}Sb_x$ bulk alloys at different concentrations of Sb are shown in Fig. 5.1. All the diffraction peaks oriented at (200), (220), (222), (400) and (420) coincided exactly with SnTe having rock salt cubic structure of *Fm-3m* space group (JCPDS No. 08-0487). The peak at (200) has the highest intensity for all Sb concentrations. Since no other peak other than that of SnTe is present in the diffraction pattern, indicating the samples have no presence of any secondary phase. However, a slight change in peak positions is observed suggesting assimilation of Fe and Sb into the SnTe matrix while retaining the crystal structure.

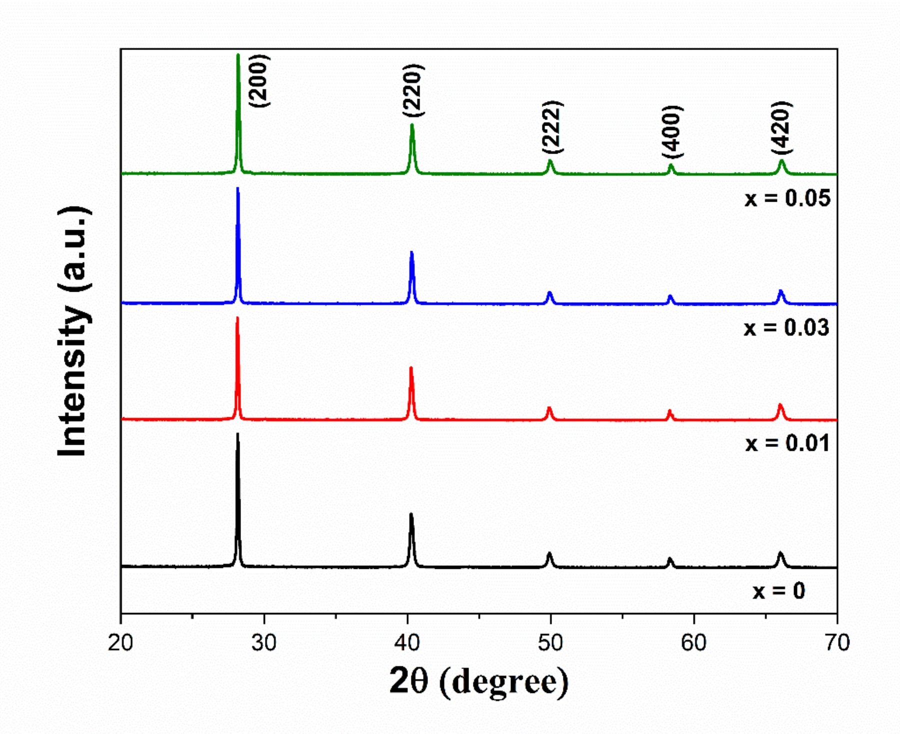

Figure 5.1: *XRD diffraction pattern with peak indexing of* $Fe_{0.05}(SnTe)_{1-x}Sb_x$ *bulk alloys for x = 0, 0.01, 0.03 and 0.05.*

From the XRD data, the values of lattice parameters of the samples have been calculated using the formula $\frac{1}{d^2} = \frac{h^2+k^2+l^2}{a^2}$ where d is interplanar spacing [29]. Further, using Scherrer's formula $D = (0.9\,\lambda) / (\beta \cos\theta)$, crystallite size (D) is also calculated. Here λ is wavelength of CuK_α radiation, θ is Bragg's angle and β is full width at half maximum (FWHM) of the diffraction peaks. The crystallite size is found to increase for x = 0 to x = 0.03 samples and then decrease for x = 0.05 sample. The values of these structural parameters are tabulated in Table 5.1.

Table 5.1: *Structural parameters calculated from XRD data.*

Samples	**From XRD**	**Crystallite Size(D)**
	a (Å)	**Nm**
$Fe_{0.05}(SnTe)$	6.330	32.215
$Fe_{0.05}(SnTe)_{0.99}Sb_{0.01}$	6.335	34.553
$Fe_{0.05}(SnTe)_{0.97}Sb_{0.03}$	6.331	34.582
$Fe_{0.05}(SnTe)_{0.95}Sb_{0.05}$	6.326	31.026

Figure 5.2 shows FESEM images of all the $Fe_{0.05}(SnTe)_{1-x}Sb_x$ powder samples. In some locations, it appears that there are stacks of layer-like structures. Over the surface of these structures are granules that seem like agglomeration of the elements present in the sample and it is seen to be more for x = 0 sample. There are irregularities in the shape of agglomerates and the surface appears to be rough. The presence of agglomerates makes it difficult to calculate exact grain size from the FESEM images.

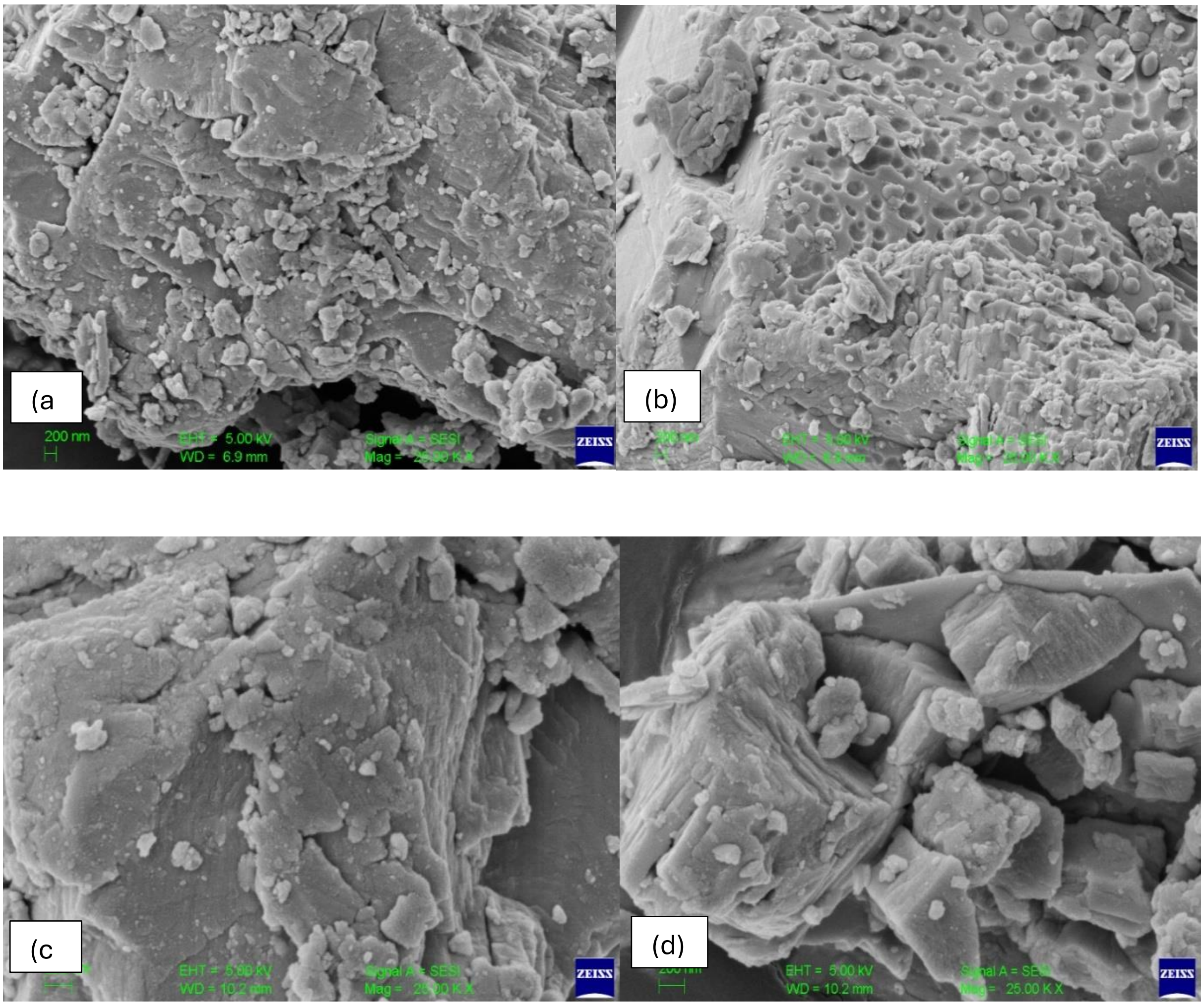

Figure 5.2: *FESEM images of $Fe_{0.05}(SnTe)_{1-x}Sb_x$ samples at (a) x = 0, (b) x = 0.01, (c) x = 0.03 and (d) x = 0.05 at 25.00 x magnification.*

5.3.2 FTIR Studies

FTIR spectra of $Fe_{0.05}(SnTe)_{1-x}Sb_x$ (x = 0, 0.01, 0.03 and 0.05) samples are shown in Fig. 5.3 recorded in the wavenumber range of 400 – 4000 cm^{-1}. The signature peaks of pure SnTe are located at 471 cm^{-1}, 647 cm^{-1}, 1619 cm^{-1}, 2381 cm^{-1} and 3430 cm^{-1} [30]. However, the peak positions of pure SnTe and their intensities have undergone a change due to doping of Fe and are labelled in the spectrum. Similarly, due to substitution of Sb, the vibration modes at 3360 cm^{-1} and 1570 cm^{-1} are found to be shifted in comparison to x = 0 sample. The purpose of recording the FTIR spectra is to calculate the band gap values of the samples. This is because the band gap value of SnTe being very small, it falls in the IR-region. Formula given below is used for this purpose.

$$(\alpha h\nu) = A(h\nu - E_g)^n \qquad (5.1)$$

Here, α represents absorption coefficient, A is a constant that is calculated from the transmittance intensity and E_g is band gap of the sample.

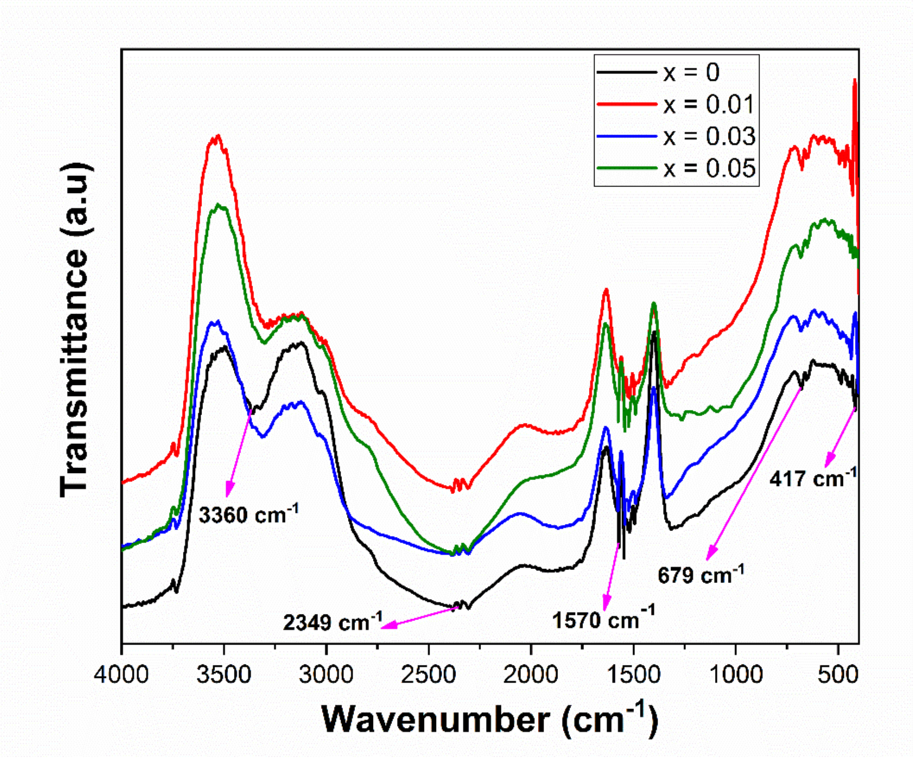

Figure 5.3: *FTIR spectra of $Fe_{0.05}(SnTe)_{1-x}Sb_x$ bulk alloys for x = 0, 0.01, 0.03 and 0.05.*

A graph of $(\alpha h\nu)^{1/n}$ *v/s* photon energy $(h\nu)$ is plotted and band gap value is determined by extrapolating the linear region of the graph in order to touch the X-axis. The value of n is taken to be ½ as SnTe has direct band gap energy. Figure 5.4 shows the plot for the same. From the literature, we have found the direct band gap of pristine SnTe to be 0.18 eV. However, in the present sample, dilute doping of Fe resulted in an increase in the band gap value to 0.21 eV. Fe has introduced holes into SnTe which has resulted in an increase in band gap value as Fermi level may have moved down into the valence band. Further, when Sb is introduced, the band gap value is found to decrease dramatically. The E_g is now 0.15 eV for x = 0.01 and 0.14 eV for x = 0.03 sample. There could be a deformation in the structure of SnTe and an impurity band level could be created into the band gap of SnTe that reduces the band gap value. On the contrary, when the concentration of Sb is increased further to x = 0.05, the band gap value is once again found to increase to 0.17 eV. This increase seems to be due to Burstein – Moss effect wherein the Fermi level is pushed into the conduction band due to increase in number of donor impurities due to Sb substitution [31, 32]. Table 5.2 lists the values of direct band gap of Fe$_{0.05}$(SnTe)$_{1-x}$Sb$_x$ samples.

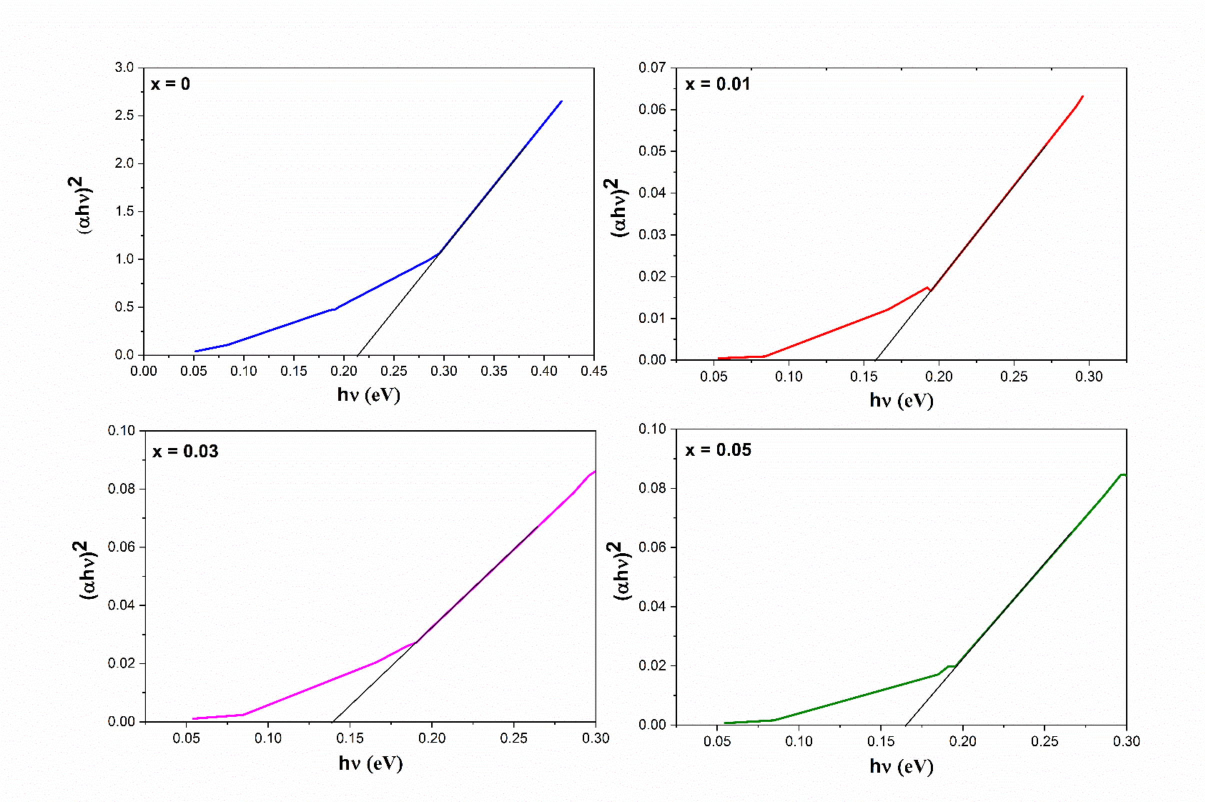

Figure 5.4: *(αhυ)^2 Vs. hυ plots of Fe$_{0.05}$(SnTe)$_{1-x}$Sb$_x$ bulk alloys to find band gap.*

Table 5.2: *Direct band gap values deduced from FTIR spectrum.*

Samples	**Direct Band Gap**
	(eV)
$Fe_{0.05}(SnTe)$	0.21 ± 0.02
$Fe_{0.05}(SnTe)_{0.99}Sb_{0.01}$	0.15 ± 0.02
$Fe_{0.05}(SnTe)_{0.97}Sb_{0.03}$	0.14 ± 0.02
$Fe_{0.05}(SnTe)_{0.95}Sb_{0.05}$	0.17 ± 0.02

5.3.3 Electrical Studies

In order to measure the effect of temperature on the resistivity of $Fe_{0.05}(SnTe)_{1-x}Sb_x$ bulk alloys, Physical Property Measurement System (PPMS) is used. The measurements of electrical resistance are carried out using the conventional Four-probe method in the temperature range of 2 K – 300 K at zero field. Additionally, an external magnetic field of 5T and 8T are also applied to note for any behavioural changes in resistivity curve. Figure 5.5(a-d) represents resistivity plots of $Fe_{0.05}(SnTe)_{1-x}Sb_x$ samples (x = 0, 0.01, 0.03 and 0.05) at 0T and external fields of 5T and 8T.

SnTe is also known to be a topological crystalline insulator [33]. From the resistivity curve of x = 0 sample in fig. 5.5(a), we can see a metal-insulator transition at temperature T_P = 190 K for 0T and 182 K for 5T fields. Doping of magnetic ion Fe acts as a hole dopant in the SnTe matrix. At 0T and 5T magnetic field, there is an increase in the interaction between charge carriers that results in charge localization and with an increase in temperature beyond transition temperature T_P, this interaction becomes weak giving rise to delocalization of charge carriers. Thus, above T_P, the sample is seen to have semiconducting nature. On increasing the magnetic field to 8T, the sample shows a predominantly semiconducting behaviour suggesting that at this high value of external magnetic field, the interaction between charge carriers become strong enough to be drifted apart. Thus, delocalization of charges take place which can be seen as a gradual decrease in the resistivity value. From the above-mentioned values of T_P, it is clear that the value reduces from 190 K for 0T to 182 K for 5T. This reduction in transition temperature could be the result of breaking of long-range ferromagnetic order in the sample. From the literature survey, we could see that a similar behaviour of decrease in transition temperature was observed in polycrystalline samples of $(Pr_{1-x}Nd_x)_{0.67}Ba_{0.33}MnO_3$ [34]. The shift in T_P value due to magnetic field could result from the presence of lattice strain in the system [35]. An additional feature that is commonly observed in the three plots is the upturn in the resistivity curve below 15 K following a minimum in the resistivity.

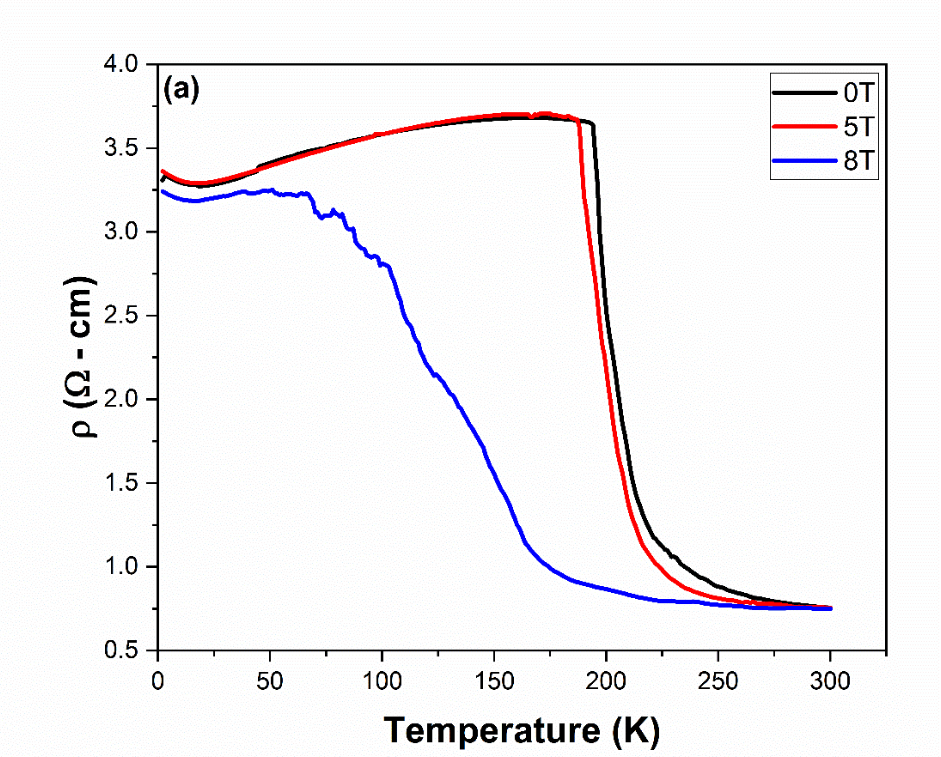

Figure 5.5(a): *Electrical resistivity of* $Fe_{0.05}(SnTe)_{1-x}Sb_x$ *bulk alloy for x = 0 at 0T, 5T and 8T.*

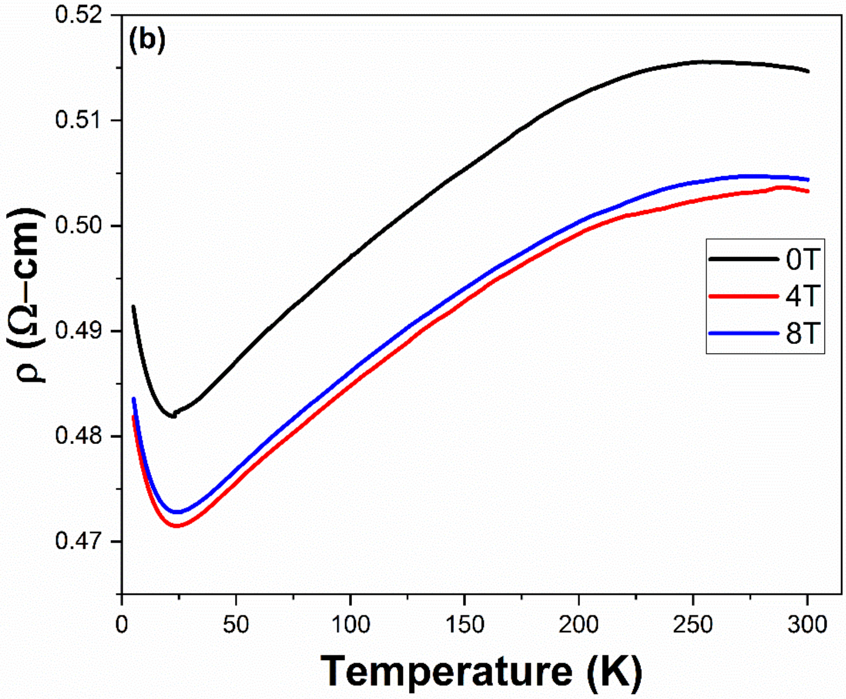

Figure 5.5(b): *Electrical resistivity of* $Fe_{0.05}(SnTe)_{1-x}Sb_x$ *bulk alloy for x = 0.01 at 0T, 5T and 8T.*

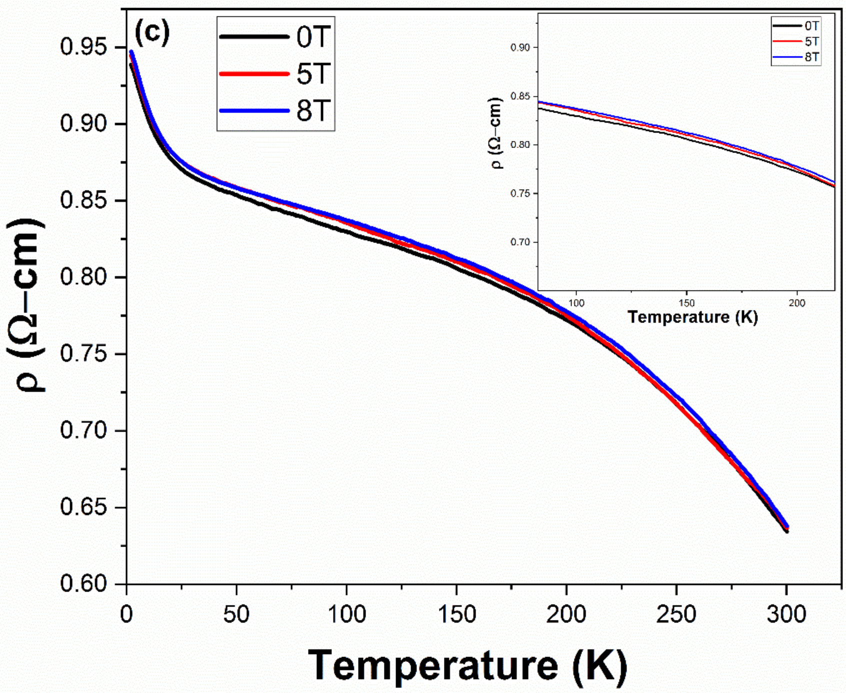

Figure 5.5(c): *Electrical resistivity of* $Fe_{0.05}(SnTe)_{1-x}Sb_x$ *bulk alloy for x = 0.03 at 0T, 5T and 8T. Magnified view of the plot is shown in the inset.*

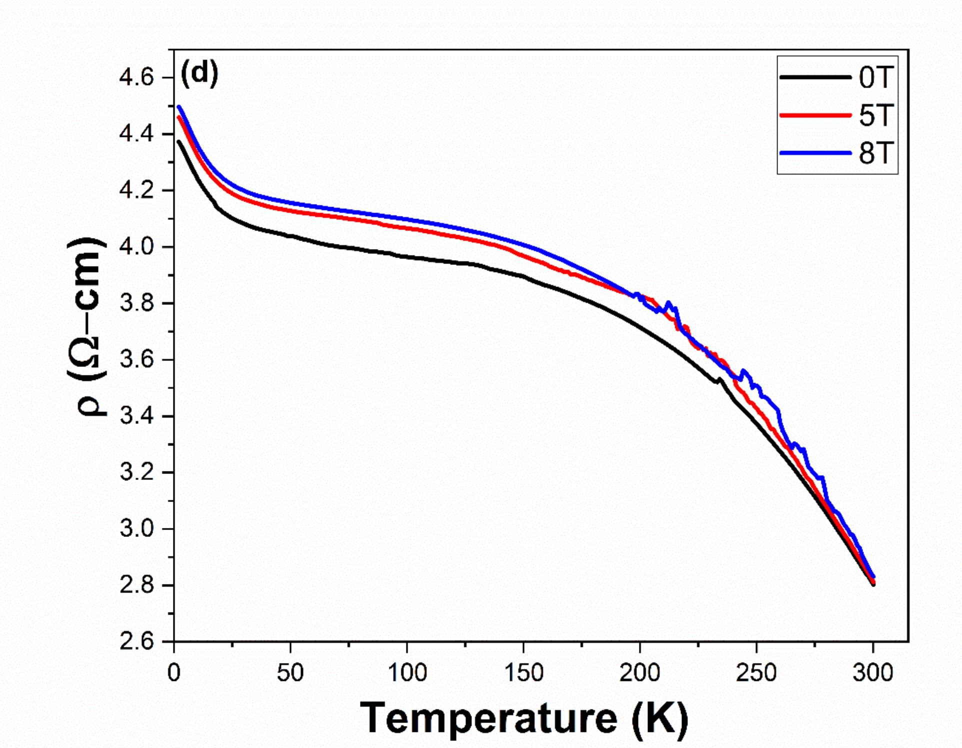

Figure 5.5(d): *Electrical resistivity of* $Fe_{0.05}(SnTe)_{1-x}Sb_x$ *bulk alloy for x = 0.05 at 0T, 5T and 8T.*

The temperature below which resistivity is seen to increase significantly is called the Kondo temperature (T_K) and the transport property of this region can be elaborated based on two factors i.e. Kondo scattering and electron – phonon scattering [36, 37]. At low temperatures, these scattering mechanisms are crucial and they are described below.

$$\rho = \rho_p T^5 - \rho_s \ln T \tag{5.2}$$

$\rho_s \ln T$ indicates the contribution from Kondo-like scattering and $\rho_p T^5$ symbolizes electron-phonon scattering for low temperatures. The low temperature data is fitted below T_K which is around 17 K down till 2 K for 0T, 5T and 8T of x = 0 sample using the above equation and the best fit is shown in Fig. 5.6(a). Applying a magnetic field has a significant impact on resistivity at low temperatures, which results in the shifting of T_K values. The parameters obtained from the fit are presented in Table 5.3.

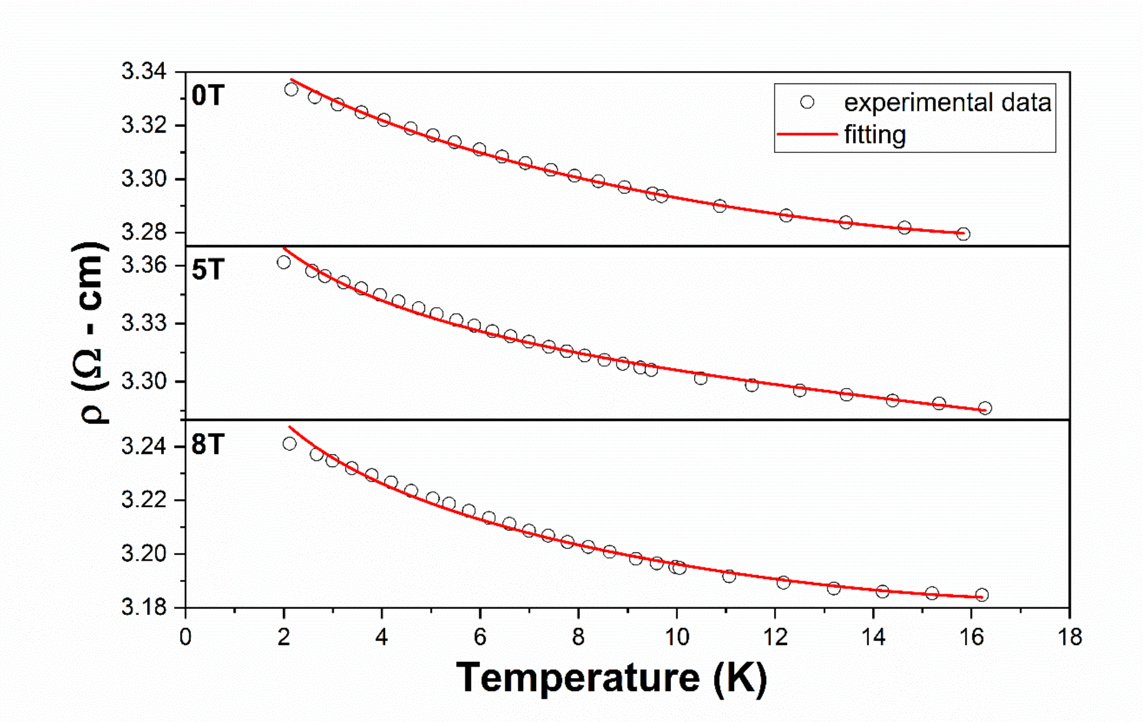

Figure 5.6(a): *Fitting of the data below Kondo temperature using equation (5.2) of* $Fe_{0.05}(SnTe)_{1-x}Sb_x$ *bulk alloy for x = 0 at 0T, 5T and 8T.*

The electrical transport mechanism of strongly correlated materials in the low temperature region of $T_K \leq T \leq T_P$ can be linked to phenomena like electron-electron scattering, two-magnon scattering and electron-electron interaction. Using the equation defined as follows, the resistivity data between the above-mentioned ranges is fitted.

$$\rho = \rho_0 + \rho_e T^{1/2} + \rho_2 T^2 + \rho_{4.5} T^{4.5} \qquad (5.3)$$

ρ_0, $\rho_e T^{1/2}$, $\rho_2 T^2$ and $\rho_{4.5} T^{4.5}$ stands for residual resistivity, electron-electron interaction, electron-electron scattering and two-magnon scattering respectively. The fitting of the above equation for 0T and 5T field resistivity data is displayed in Fig. 5.6(b). Since there is no sharp transition from metallic to semiconducting behaviour in the resistivity data for 8T field, it is also fitted using equation (5.3) in the temperature range from 20 K – 40 K below the semiconducting region as shown in Fig. 5.6(c). The parameter values are presented in Table 5.3.

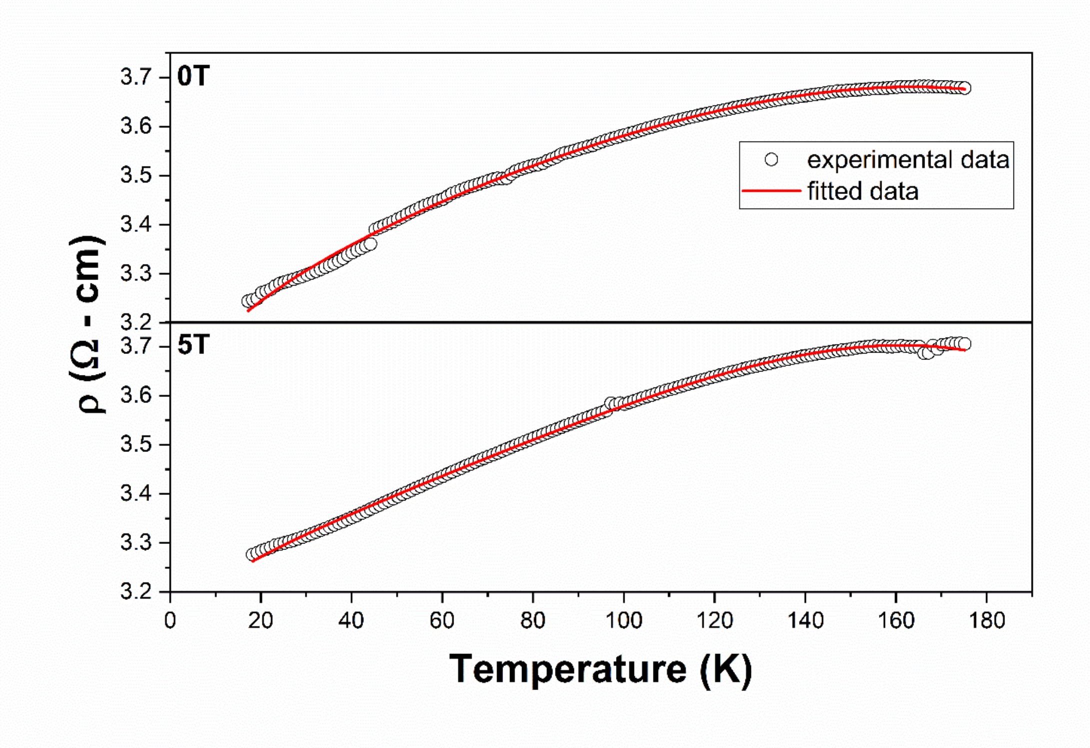

Figure 5.6(b): *Fitting of the resistivity data of* $Fe_{0.05}(SnTe)_{1-x}Sb_x$ *bulk alloy for* $x = 0$ *between* $T_K \leq T \leq T_P$ *at 0T and 5T using equation (5.3).*

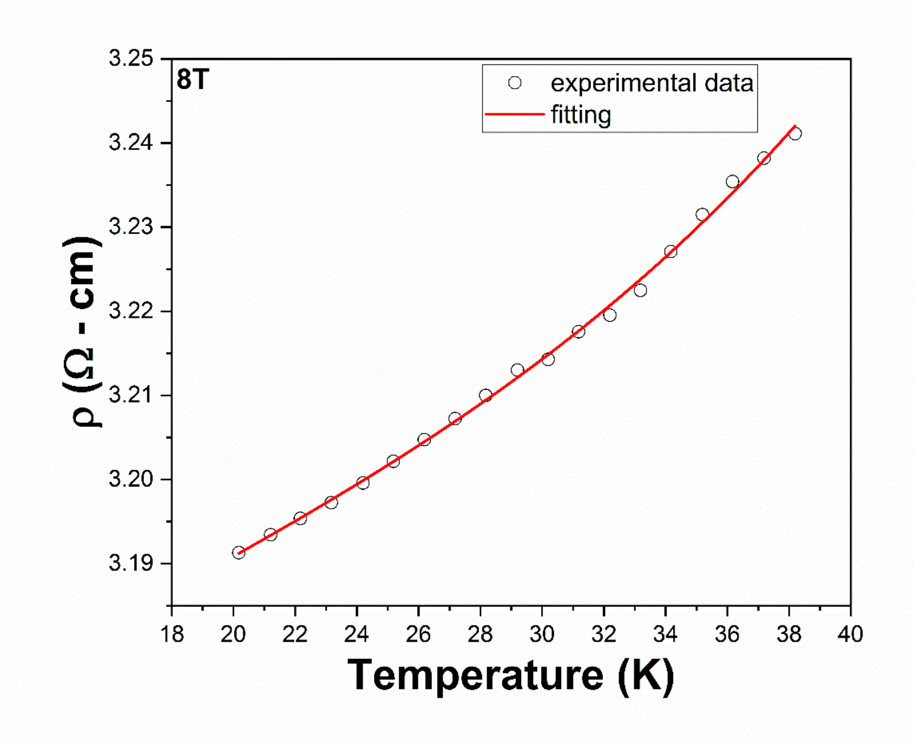

Figure 5.6(c): *Fitting of the resistivity data of* $Fe_{0.05}(SnTe)_{1-x}Sb_x$ *bulk alloy for* $x = 0$ *below semiconducting region at 8T using equation (5.3).*

Table 5.3: *Fitting parameters for* $Fe_{0.05}(SnTe)_{1-x}Sb_x$*; x = 0 sample.*

Applied Magnetic Field	**Parameters from eq. 5.2**		**Parameters from eq. 5.3**			
	ρ_p **x10^{-9} (Ω.cm/K^5)**	ρ_s **(Ω.cm)**	ρ_0 **(Ω.cm)**	ρ_e **(Ω.cm/K$^{1/2}$)**	ρ_2 **(Ω.cm/K^2)**	$\rho_{4.5}$ **(Ω.cm/K$^{4.5}$)**
0T	5.831	0.0447	2.970	0.0613	8.89×10^{-7}	-1.06×10^{-11}
5T	1.406	0.0393	3.089	0.0398	1.14×10^{-5}	-2.18×10^{-11}
8T	3.581	0.0331	3.129	0.0013	1.01×10^{-5}	1.51×10^{-9}

The value of $\rho_{4.5}$ is negative for 0T and 5T fields signifying weak contribution of two-magnon scattering as compared to other factors. For 8T field, all factors contribute equally to its transport mechanism.

The resistivity plot of x = 0.01 sample, however, shows an increasing trend till about 250 K which is the feature of a metallic nature. Above this temperature, the plot is seen to saturate. Similar to the resistivity plot of x = 0 sample, an upturn in the resistivity value is observed on lowering the temperature below a minimum around 23 K, known as Kondo temperature (T_K). This is the Kondo effect and as described above, in addition to Kondo scattering, electron – phonon interaction also contributes to the transport property at such low values of temperature. The plots fitted with equation (5.2) is shown in Fig. 5.7(a) and the parameters are presented in Table 5.4. Similarly, above T_K, transport mechanism of the sample can be explained using terms that concern with electron-electron scattering, two-magnon scattering and electron-electron interaction which when combined form an equation as expressed in equation (5.3) and the fitting to the resistivity curve is shown in Fig. 5.7(b). Table 5.4 also displays the parameter values of x = 0.01 sample obtained from the above fitting.

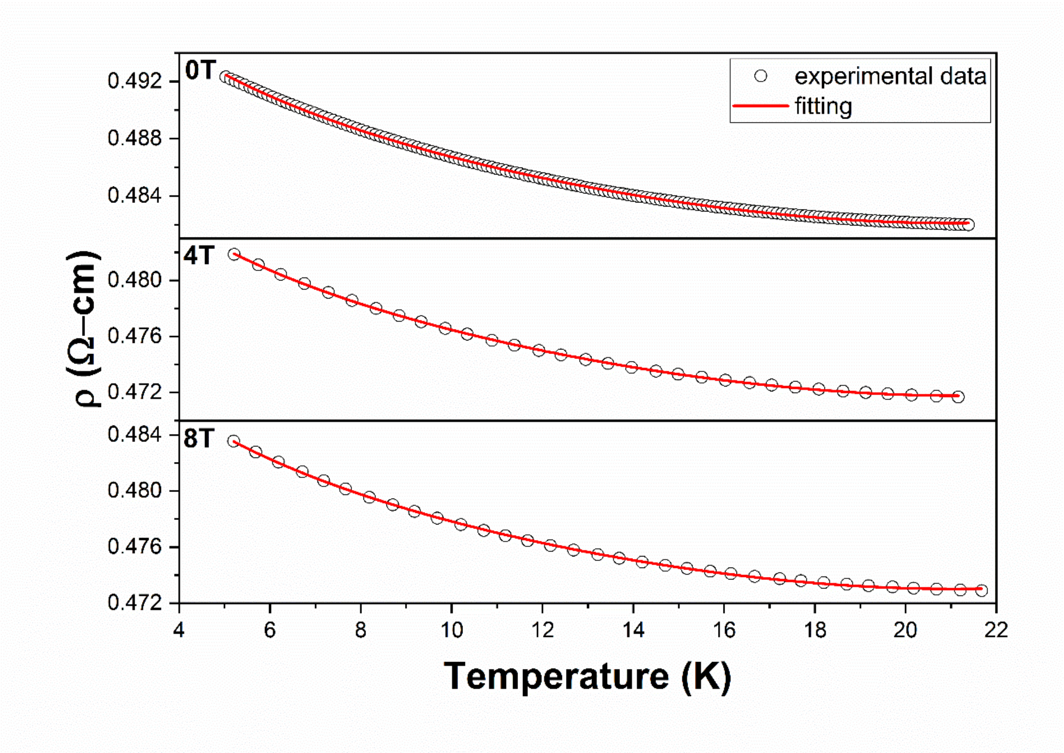

Figure 5.7(a): *Fitting of the data below Kondo temperature of* $Fe_{0.05}(SnTe)_{1-x}Sb_x$ *bulk alloy for x = 0.01 using equation (5.2) at 0T, 5T and 8T.*

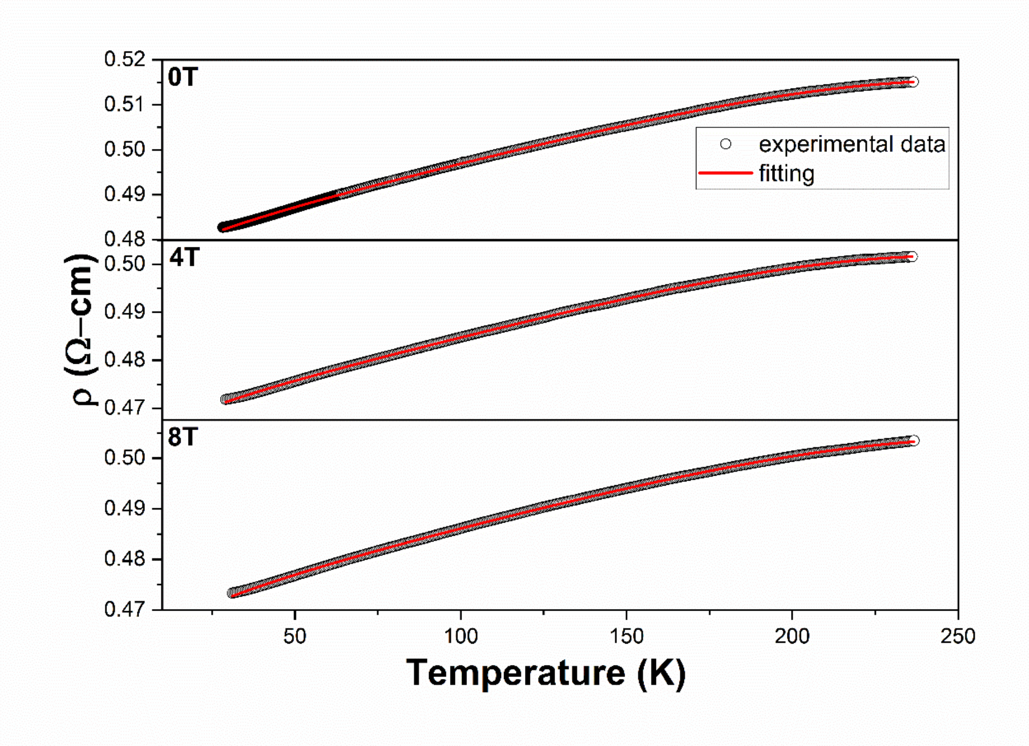

Figure 5.7(b): *Fitting of the resistivity data of* $Fe_{0.05}(SnTe)_{1-x}Sb_x$ *bulk alloy for x = 0.01 above Kondo temperature at 0T, 5T and 8T using equation (5.3).*

Table 5.4: *Fitting parameters for* $Fe_{0.05}(SnTe)_{1-x}Sb_x$*;* $x = 0.01$ *sample.*

Applied Magnetic Field	**Parameters from eq. (5.2)**		**Parameters from eq. (5.3)**			
	ρ_p **x10**$^{-10}$ **(Ω.cm/K**^{5}**)**	ρ_s **(Ω.cm)**	ρ_0 **(Ω.cm)**	ρ_e **(Ω.cm/K**$^{1/2}$**)**	ρ_2 **x10**$^{-7}$ **(Ω.cm/K**^{2}**)**	$\rho_{4.5}$ **x10**$^{-13}$ **(Ω.cm/K**$^{4.5}$**)**
0T	4.606	0.0084	0.486	0.0026	3.190	-2.136
4T	4.443	0.0085	0.458	0.0023	3.145	-2.203
8T	4.244	0.0088	0.448	0.0026	2.353	-1.602

The value of $\rho_{4.5}$ is seen to be negative in the sample which implicates weak contribution of two-magnon scattering for all field values. From the table, the fitted values of some parameters are also seen to decrease with increase in magnetic field. This suggests that presence of magnetic field suppresses those interactions and scattering processes that take place within the sample.

In the case of x = 0.03 and 0.05 samples, the resistivity curve drops considerably with increasing temperature for different external field values. This illustrates semiconducting behaviour even though the nature of the plot is not what it is for a conventional semiconductor. At the lower temperature region of the plot, an upsurge in the resistivity value is observed below 25 K for both the samples in the presence and absence of external field. This is a signature of a transition to insulating state, the origin of which seems to be due to localization effects of the charge carriers as no tremendous change is observed in the resistivity value is observed with the application of magnetic field.

From the resistivity data of x = 0, 0.03 and 0.05 samples, the transport property has also been analyzed using different conduction models like thermal activation energy model, nearest neighbour hopping (NNH), small polaron hopping (SPH) model and variable range hopping (VRH) model. These models govern a specific range of temperature, and their validity is checked from the linear fit made to the plots that represent each of the respective models. As the samples present a resistivity curve that does not represent a conventional semiconductor, the aforesaid transport models can only be reliable for a narrow range of temperatures. SPH model came across as an absolute fit to explain the conductivity mechanism in the high temperature region. The theory and equation representing SPH model has been well explained in the previous chapter 3. $x = 0.01$ sample being metallic in the temperature window of measurement, the transport mechanism of the sample is inexplicable by the above hopping models.

In $x = 0$ sample, the region above T_P of the resistivity data that is insulating in nature is where SPH model finds its credibility. The temperature range within which it is valid is roughly from 260 K – 300 K which is quite small as seen in Fig. 5.8(a). Meanwhile, in $x = 0.03$ and 0.05 samples, alongside SPH model, NNH model is also found to hold true in the same window of temperature. This hints at the likelihood that more than one of the above-stated models describes the transport mechanism of the two samples, each of which contributes to the conduction of the carriers. We, however, only present the SPH model plot $ln(\rho/T)$ v/s T^{-1} of $x = 0.03$ and 0.05 samples in Fig. 5.8(b) and (c) respectively. The activation energy values for hopping conduction are deduced from the slope of the linear fit to the data and they are found to be decreasing with applied magnetic field values as listed in Table 5.5. This is because on application of magnetic field, there is an increase in the interaction between magnetic field and Fe ion spins that gets aligned thereby decreasing the effective mass of conduction electrons [38]. As a result, activation energy required for the hopping of conduction electrons also decreases.

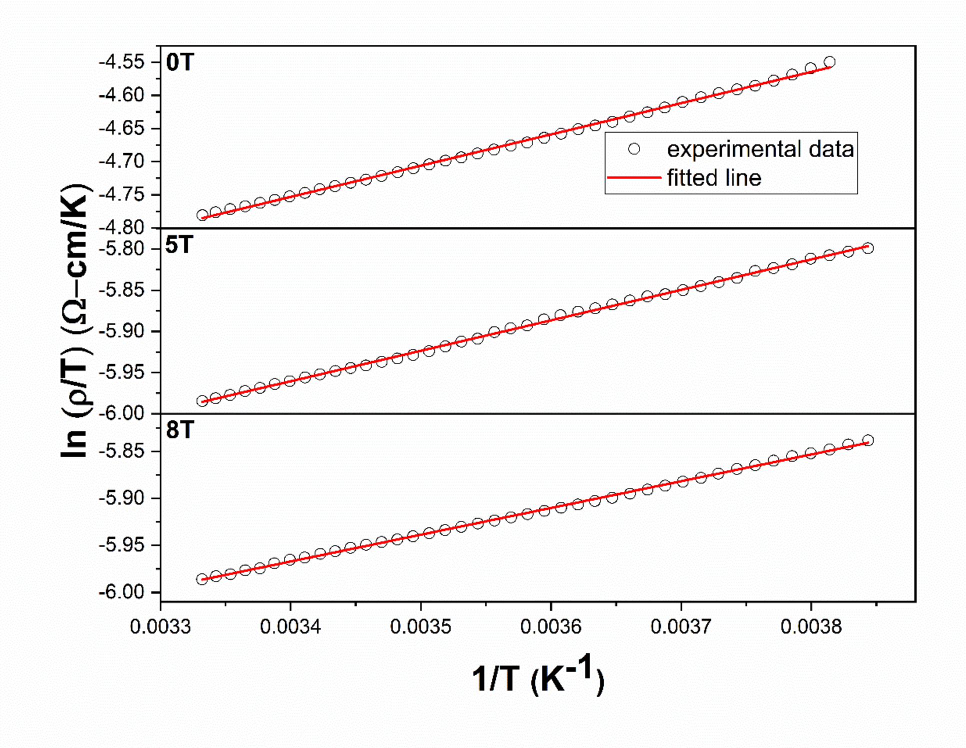

Figure 5.8(a): *Fitting of SPH model in the temperature range 260 K – 300 K of x = 0 sample.*

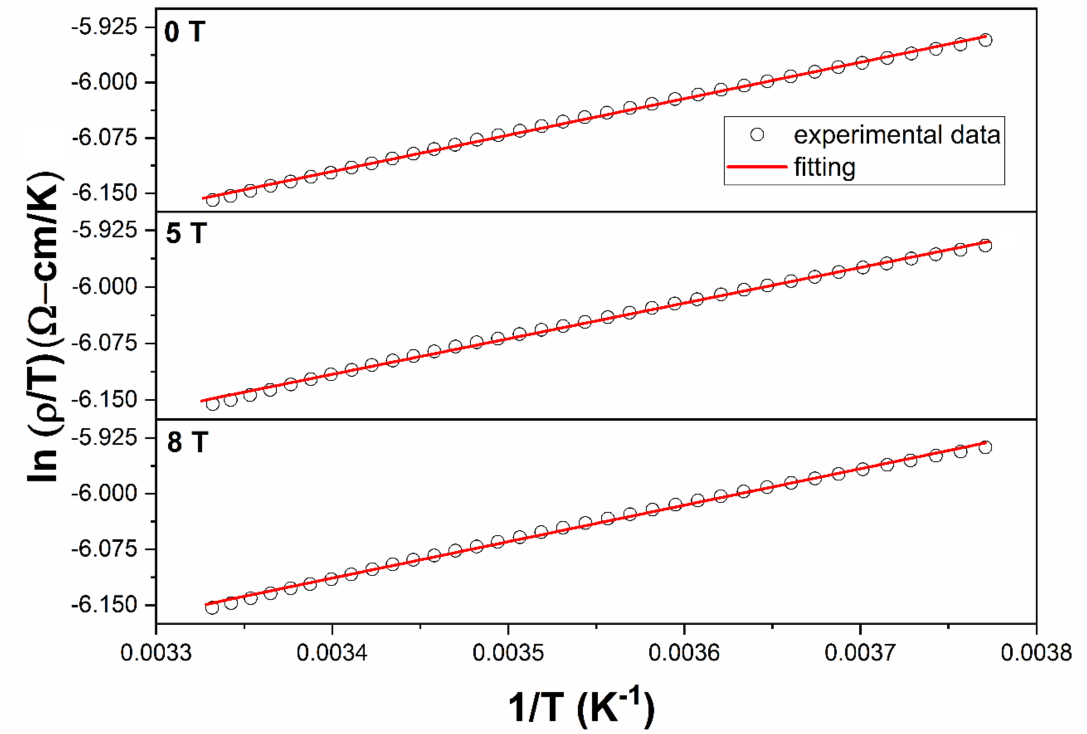

Figure 5.8(b): *Fitting of SPH model in the temperature range 260 K – 300 K of x = 0.03 sample.*

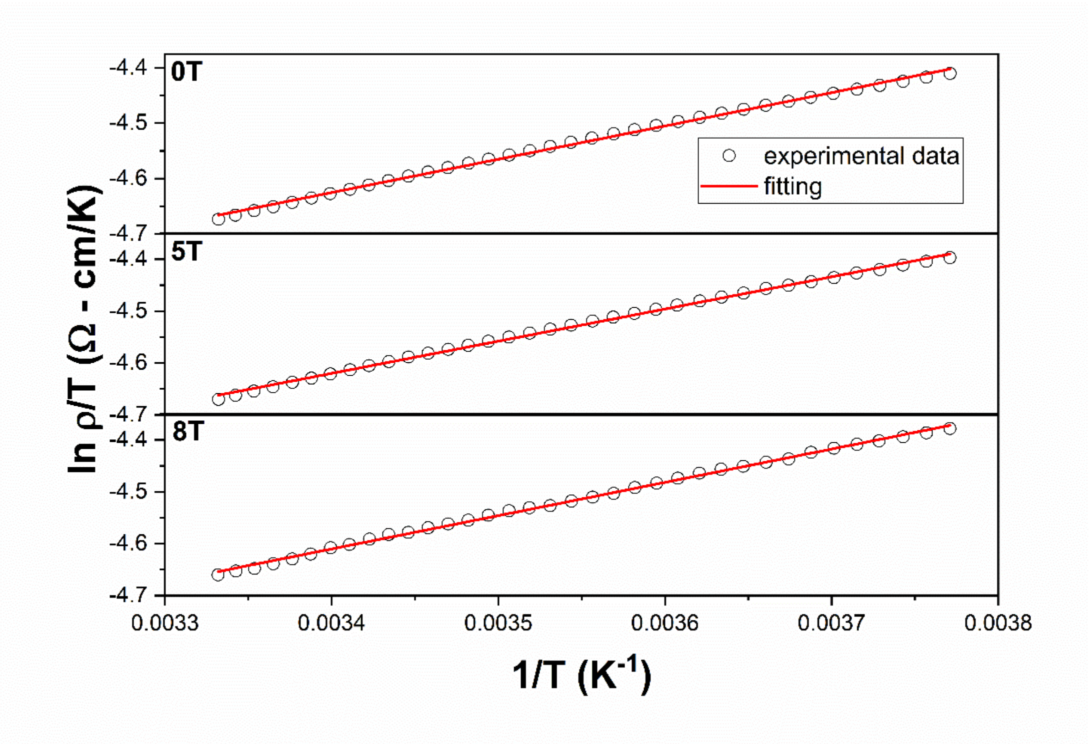

Figure 5.8(c): *Fitting of SPH model in the temperature range 260 K – 300 K of x = 0.05 sample.*

Table 5.5: *Activation energy (Ea) values from SPH model fitting to the high temperature region.*

Samples	**E_a values (meV)**		
	Applied Magnetic Field		
	0T	**5T**	**8T**
$Fe_{0.05}(SnTe)$	80.25	63.89	31.47
$Fe_{0.05}(SnTe)_{0.97}Sb_{0.03}$	42.42	41.72	40.62
$Fe_{0.05}(SnTe)_{0.95}Sb_{0.05}$	52.11	51.95	51.00

SPH model is unable to account for the transport properties of the resistivity data at low regions of temperatures. Further analysis led to VRH model being found reliable in the low range of temperatures. In Chapter 3, the three-dimensional VRH model has been thoroughly explained on the basis of which a plot of $ln\ (\rho)$ v/s $T^{-1/4}$ is made as shown in Fig. 5.9(a, b). A fit is made in the linear region of the graph and from the slope we calculate the value of Mott's temperature T_0. T_0 is the characteristic temperature which has a direct correlation with the average energy that is required for localized charge carriers to hop to their nearest neighbouring site. For x = 0 sample, the VRH model is not supported as low temperature conduction mechanism. It seems there could be a combination of different conduction mechanisms that would explain the transport property at low temperature. x = 0.03 and 0.05 sample is seen to hold VRH model in the range 3 K – 85 K and 5 K – 40 K respectively. From the values given in Table 5.6, we see a minuscule decrease in T_0 with magnetic field for all the samples. This decrease in T_0 can be correlated to density of states $N(E_F)$ increasing at the Fermi level which is considered to be favourable for hopping of charge carriers.

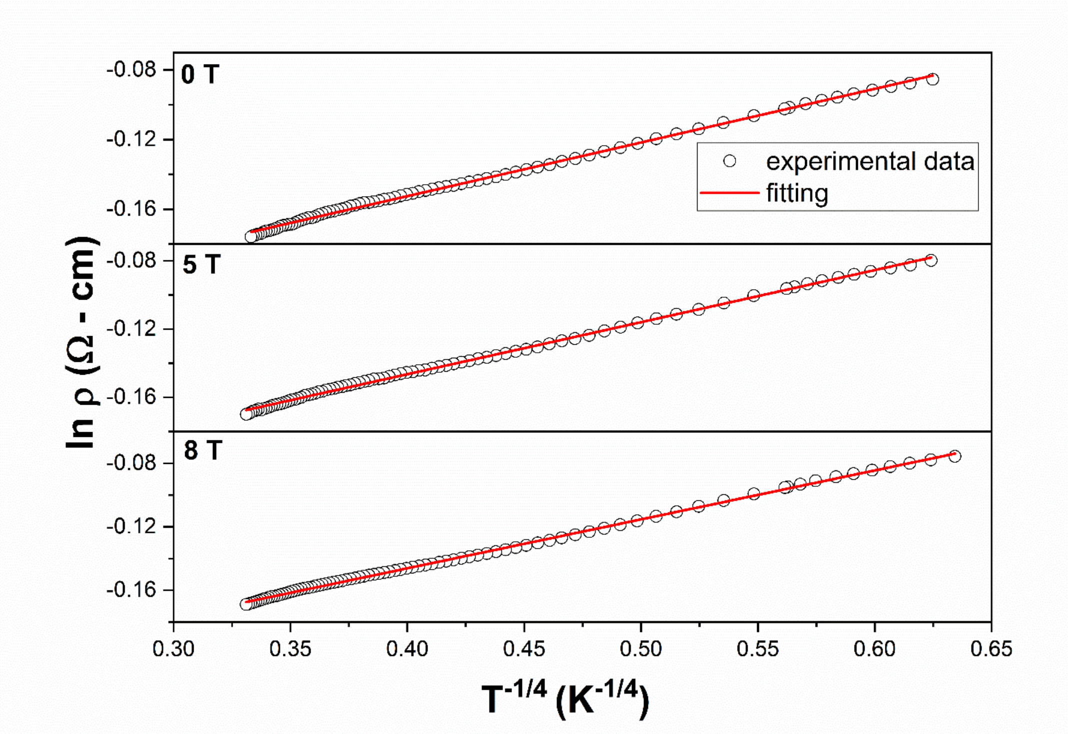

Figure 5.9(a): *Fitting of VRH model in the temperature region from 3 K – 85 K of x = 0.03 sample.*

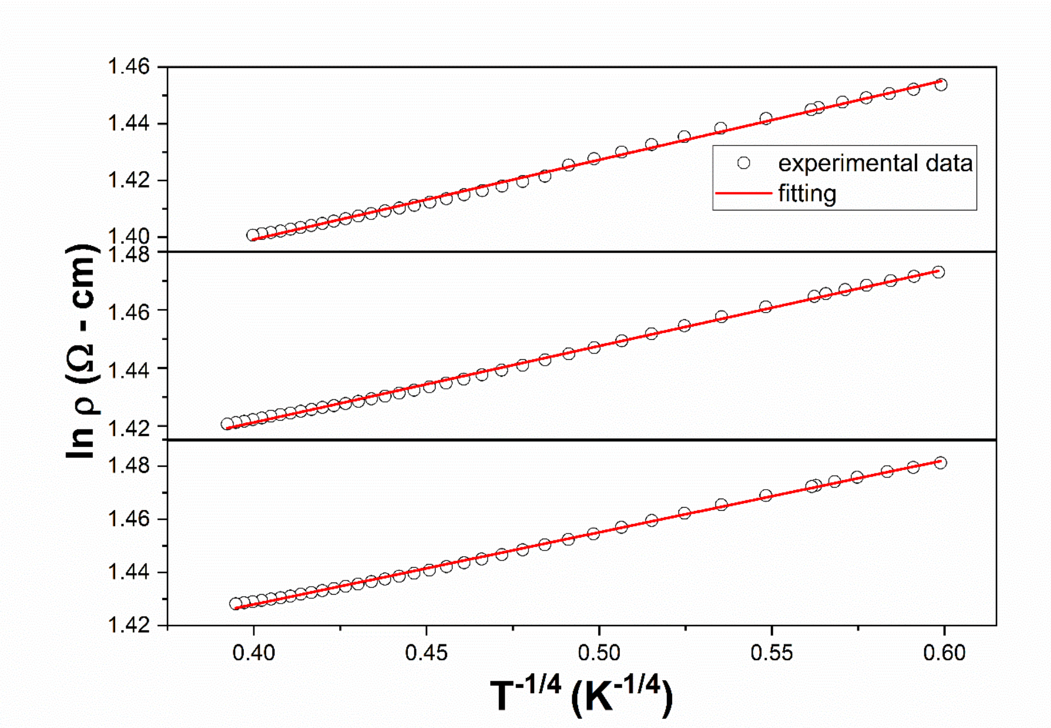

Figure 5.9(b): *Fitting of VRH model in the temperature region from 5 K – 40 K of x = 0.05 sample.*

Table 5.6: *Mott's temperature (T_0) derived from VRH model fitting to the low temperature region.*

Samples	T_0 values (*K*)		
	Applied Magnetic Field		
	0T	**5T**	**8T**
$Fe_{0.05}(SnTe)_{0.97}Sb_{0.03}$	90.23 x 10^{-4}	82.63 x 10^{-4}	78.65 x 10^{-4}
$Fe_{0.05}(SnTe)_{0.95}Sb_{0.05}$	69.36 x 10^{-4}	54.37 x 10^{-4}	53.43 x 10^{-4}

5.3.4 Magnetotransport Studies

Electrical resistivity measured in the presence and absence of an externally applied magnetic field is known as magnetoresistance. It is defined by the equation

$$M(R)\% = \frac{\rho(H,T) - \rho(0,T)}{\rho(0,T)} \times 100 \tag{5.4}$$

where $\rho(H, T)$ and $\rho(0, T)$ are resistivity values in the presence and absence of an applied field H respectively for a given temperature T. When a magnetic material is exposed to a magnetic field, the localized spins may fluctuate, which causes magnetic scattering, which in turn causes magnetoresistance. Magnetoresistance measurement of $Fe_{0.05}(SnTe)_{1-x}Sb_x$ bulk alloys (x = 0, 0.01, 0.03 and 0.05) is carried out using Physical Property Measurement System (PPMS) in the magnetic field range up to 8 T at temperatures 5, 10, 15, 25, 50 and 100 K and are shown in Fig. 5.10(a-d).

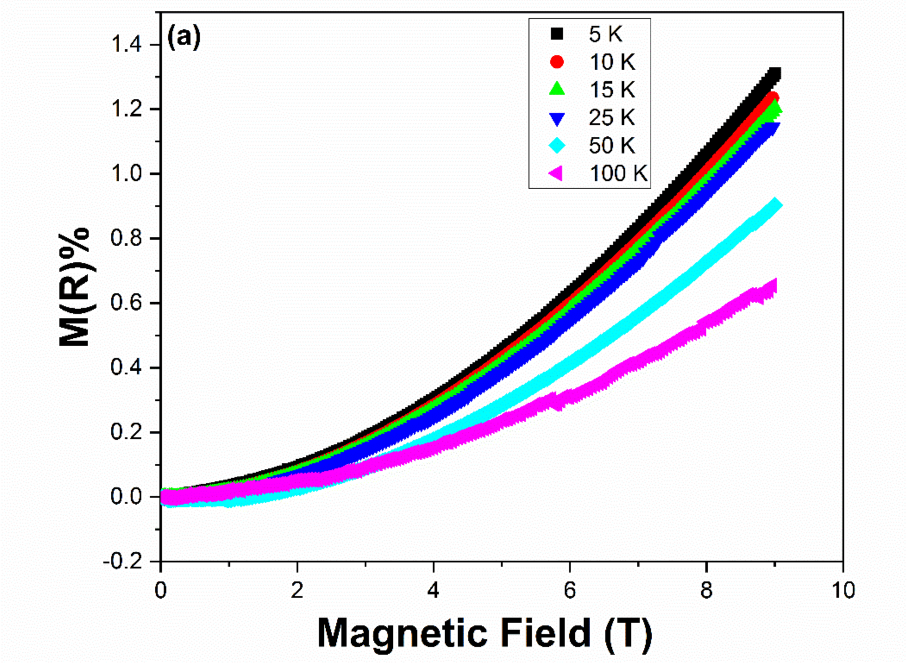

Figure 5.10(a): *Magnetoresistance plot of* $Fe_{0.05}(SnTe)_{1-x}Sb_x$ *bulk alloy for x = 0.*

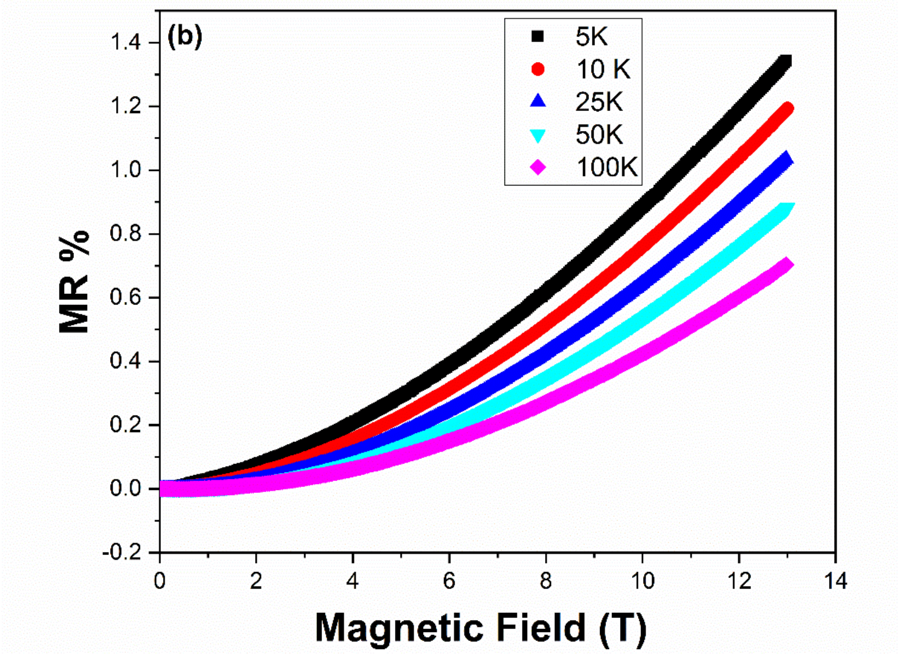

Figure 5.10(b): *Magnetoresistance plot of* $Fe_{0.05}(SnTe)_{1-x}Sb_x$ *bulk alloy for x = 0.01.*

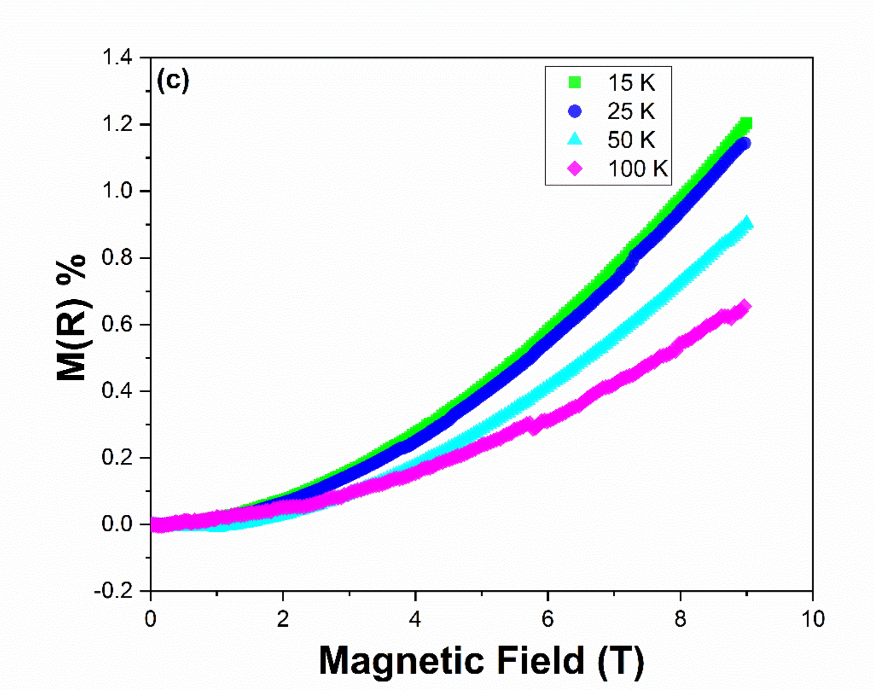

Figure 5.10(c): *Magnetoresistance plot of* $Fe_{0.05}(SnTe)_{1-x}Sb_x$ *bulk alloy for* $x = 0.05$.

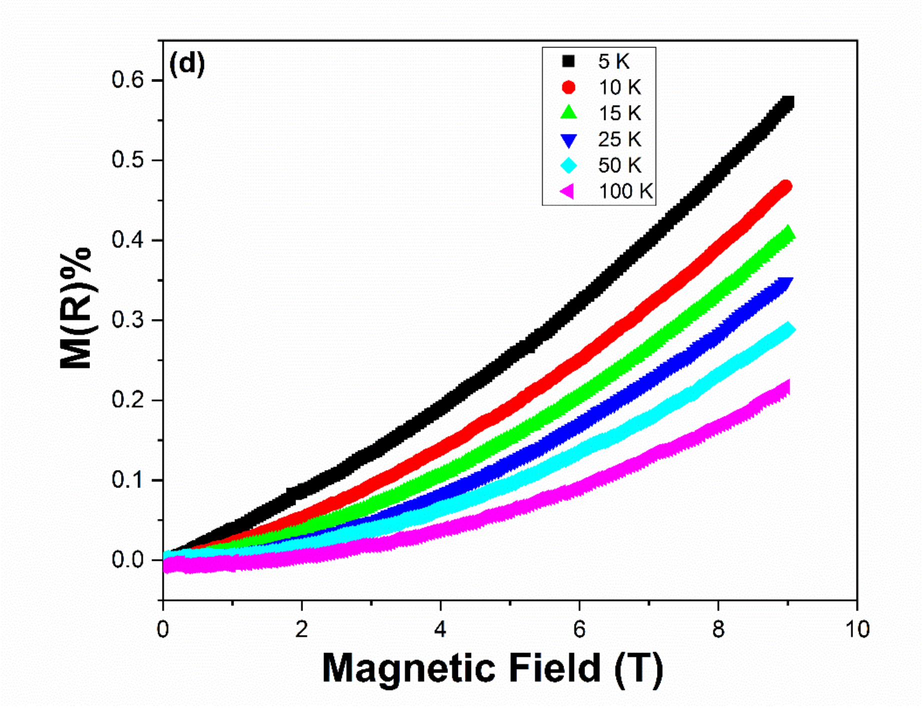

Figure 5.10(d): *Magnetoresistance plot of* $Fe_{0.05}(SnTe)_{1-x}Sb_x$ *bulk alloy for* $x = 0.05$.

All the samples are seen to exhibit positive magnetoresistance at all temperatures which is typically anticipated for hopping conduction. The MR% value is seen to decrease from 1.3% for 5 K to 0.6% for 100 K, 1.35% for 5 K to 0.7% for 100 K, 1.2% for 15 K to 0.6% for 100 K and 0.6% for 5 K to 0.2% for

100 K for x = 0, 0.01, 0.03 and 0.05 samples respectively. The positive magnetoresistance can be explained on the basis of wave shrinkage model [39]. Application of magnetic field localizes the charge carriers. With an increase in magnetic field strength, there is contraction of the wave function of these localized electrons as well as the wave function of the neighbouring sites. This reduces the overlapping of these two wave functions thereby reducing the likelihood of electron hopping to the site. As a result, conduction of electrons decreases resulting in an increase in resistivity. In addition, a linear unsaturated behaviour is also visible in the MR curve above 6 T. Such an unsaturated linear magnetoresistance has been observed in modestly doped narrow band gap semiconductors like $Ag_2(Se,Te)$ and GaAs as well as in Bi_2Te_3 nanosheets, Bi_2Se_3 and YSi single crystal [40-44]. Such a behaviour could be the result of inhomogeneity that leads to a disorder in the carrier mobility in the crystal which causes an increase in MR% with increasing magnetic field. Materials that are topological insulators in nature having smaller values of band gap with positive magnetoresistance can find suitable applications in an emerging field of topological spintronics.

5.3.5 Magnetic Studies

DC magnetization study of the samples were performed using super conducting quantum interface device – vibrating sample magnetometer (SQUID-VSM) system. The measurements were carried out in the temperature range of 10 K – 300 K up to 8 T range of magnetic field. Magnetic moment v/s temperature (M-T) measurements were performed under zero field cooling (ZFC) and field cooling (FC) conditions. In ZFC condition, cooling of sample takes place without any external magnetic field till 10 K. At this point, a magnetic field of 200 Oe is applied to the sample and it is heated from 10 K till 300 K simultaneously recording the variation in magnetic moment. However, in FC condition, cooling of sample already takes place in the presence of magnetic field of 200 Oe till 10

K. And once again, the sample is heated till 300 K in the presence of this magnetic field alongside noting the magnetic moment variation with temperature. Figure 5.11(a-d) represents M – T plots under ZFC-FC condition of $Fe_{0.05}(SnTe)_{1-x}Sb_x$ samples (x = 0, 0.01, 0.03 and 0.05).

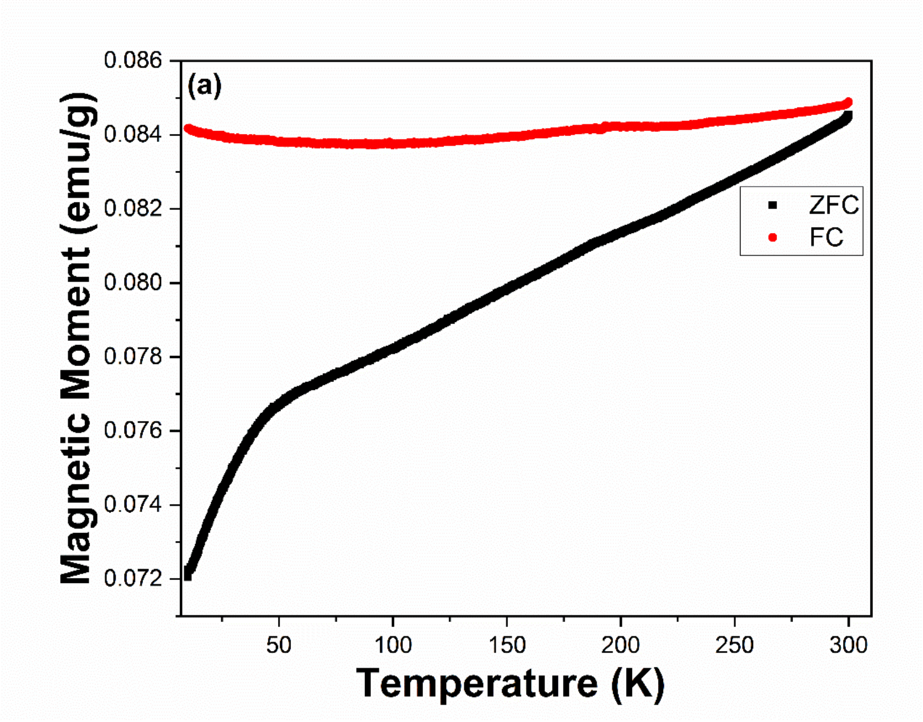

Figure 5.11(a): *M-T plot under ZFC-FC conditions of* $Fe_{0.05}(SnTe)_{1-x}Sb_x$ *bulk alloy for x = 0.*

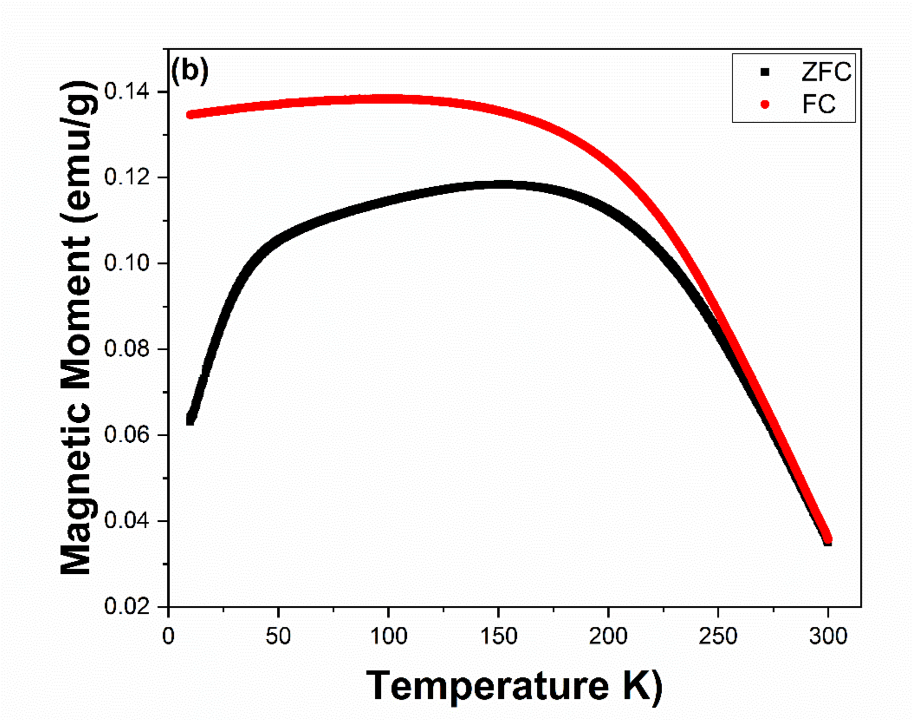

Figure 5.11(b): *M-T plot under ZFC-FC conditions of* $Fe_{0.05}(SnTe)_{1-x}Sb_x$ *bulk alloy for x = 0.01.*

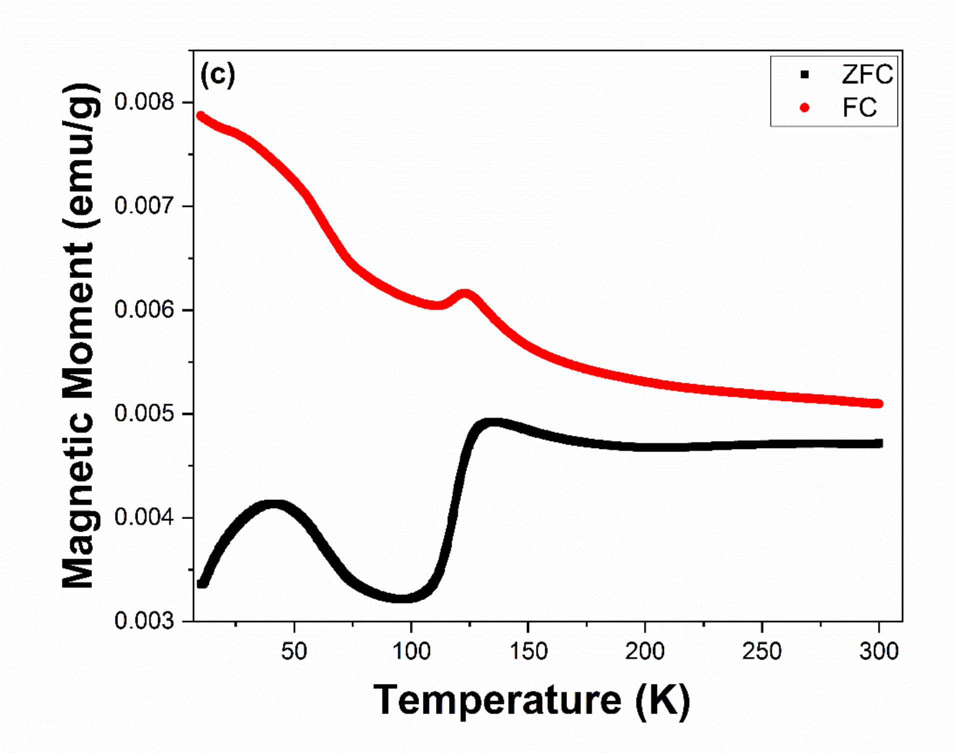

Figure 5.11(c): *M-T plot under ZFC-FC conditions of* $Fe_{0.05}(SnTe)_{1-x}Sb_x$ *bulk alloy for x = 0.03.*

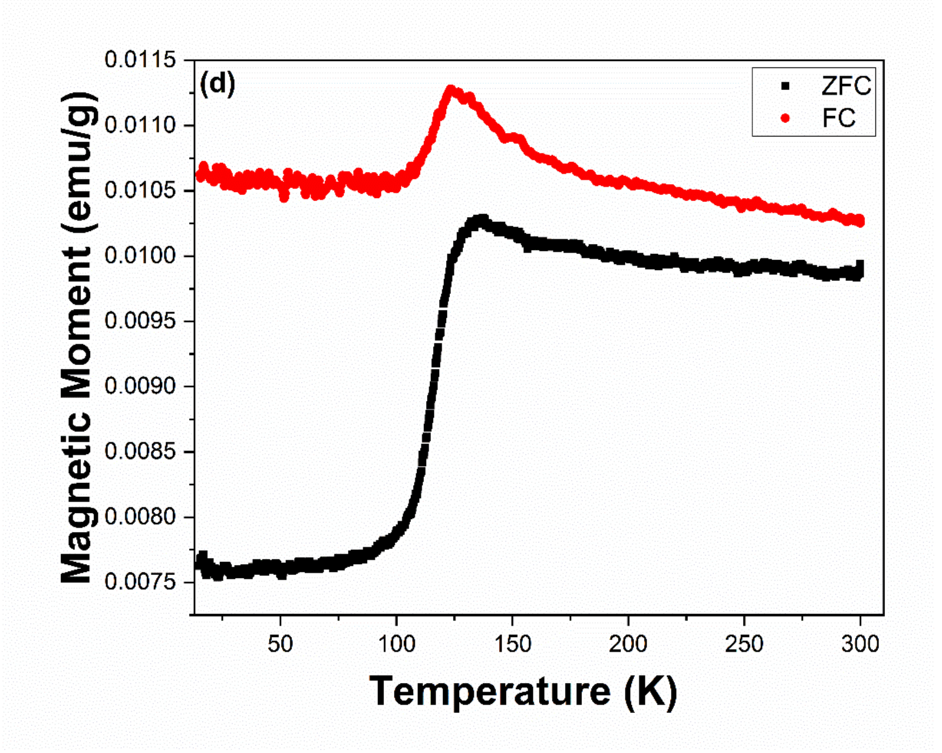

Figure 5.11(d): *M-T plot under ZFC-FC conditions of* $Fe_{0.05}(SnTe)_{1-x}Sb_x$ *bulk alloy for x = 0.05.*

x = 0 sample demonstrates thermal irreversibility as evident from the bifurcation between ZFC and FC curves below 300 K. Also, there is a sudden drop in magnetization that is observed around 50 K in the ZFC curve. The weak presence of spin-glass state that results from the freezing of spins may be the cause of this behaviour [45]. On the other hand, the FC curve seems to be fairly constant in nature throughout the entire temperature range. This is suggestive of presence of a strong inter-particle coupling. The ZFC curve of x = 0.01 sample reaches a maximum at around 200 K known as blocking temperature (T_b) beyond which both the ZFC and FC curve overlap each other accompanied by a decrease in the moment value. This is the signature of superparamagnetic feature in the sample. At lower values of temperature, the drop in the moment value suggests either antiferromagnetic or spin-glass state in the system. In the case of x = 0.03 sample, one can see a distinct magnetic transition from one state to another. The ZFC and FC curves both show a sharp cusp at about 132 K, which is suggestive of an antiferromagnetic transition in the system. The cusp could arise due to some antiferromagnetic phase of Fe-Sb [46]. Another cusp is also to be seen in the ZFC curve at roughly 50 K which may have its origin in the antiferromagnetic FeTe phase [47]. As the temperature drops below 113 K, we can see the moment value of FC curve rising signifying ferromagnetic transition. Also, the large bifurcation between ZFC and FC curves indicates a distinguishing feature of magnetic glassy state i.e. either a spin-glass state or cluster-glass state [48]. In such states, the spin-orientations in the sample that are randomly arranged undergo freezing at lower temperatures. On a similar note, the ZFC – FC curves of x = 0.05 sample is also seen to show a cusp at around 135 K indicating anti-ferromagnetic behaviour that could have its origins in the antiferromagnetic phase of Fe-Sb as seen for x = 0.03 sample also. Beyond this temperature, there is a decrease in the magnetization values which is suggestive of ferromagnetic behaviour. Another prominent feature in x = 0.05 is the presence of large bifurcation between ZFC and FC curves below 125 K. This bifurcation can be attributed to thermodynamic irreversibility [49]. This may be the result of intense competitive interactions between ferromagnetic and antiferromagnetic phases due to randomized blocking of magnetic moments.

Magnetic properties are further explored through plotting of magnetization loops of the samples that is represented by the M-H curve. The measurements were performed at desirable temperatures in the range of applied field from -70 kOe to 70 kOe. In x = 0 sample, the M-H curve was recorded at temperatures 10 K and 300 K as shown in Fig. 5.12(a). At lower values of applied field, the curves show presence of hysteresis and at higher field values, the curves are found to be saturated thereby manifesting ferromagnetic behaviour. The value of saturation magnetization (M_s) for the curves at 10 K and 300 K are ~0.7 emu/gm and ~0.54 emu/gm respectively. A similar decrease is also observed in coercivity values from 133 Oe at 10 K to 105 Oe at 300 K. Presence of holes through doping of Fe play a vital role in mediating an indirect exchange interaction between Fe^{2+} ions thereby establishing magnetic behaviour in the sample.

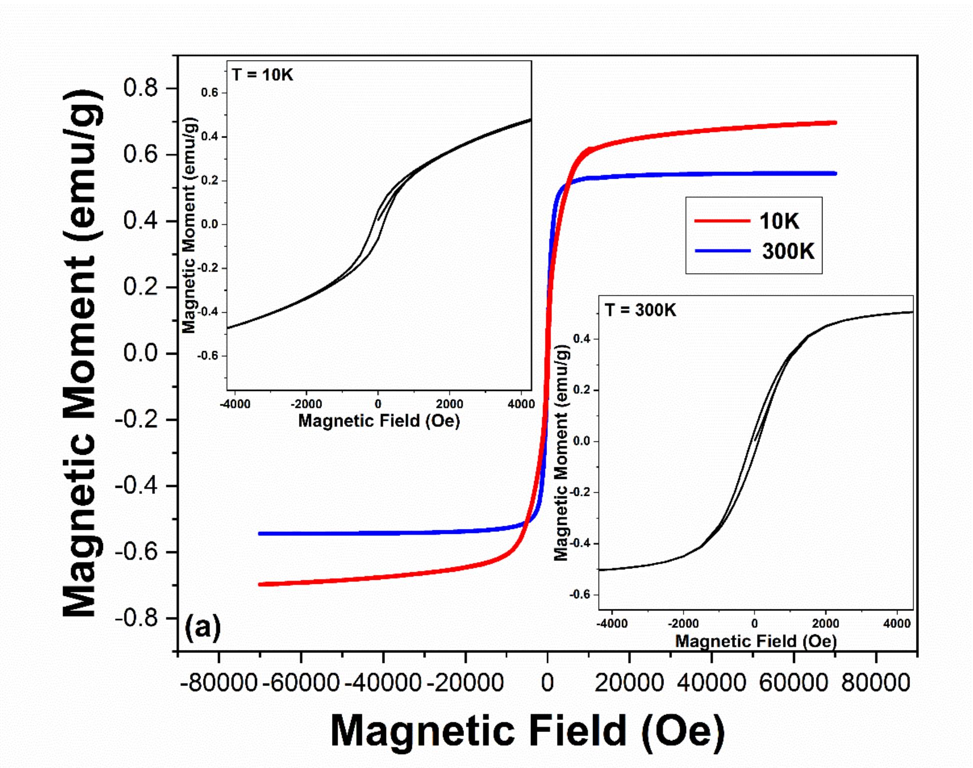

Figure 5.12(a): *M-H plot at 10K and 300K of* $Fe_{0.05}(SnTe)_{1-x}Sb_x$ *bulk alloy for x = 0.*

The M-H curve of x = 0.01 sample as seen in Fig. 5.12(b) measured at 50 K represents antiferromagnetic feature and the coercivity value also decreases when compared to the previous case. Superparamagnetic behavior as reckoned from M-T curve is also confirmed from the M-H curve at 300 K which shows zero coercivity.

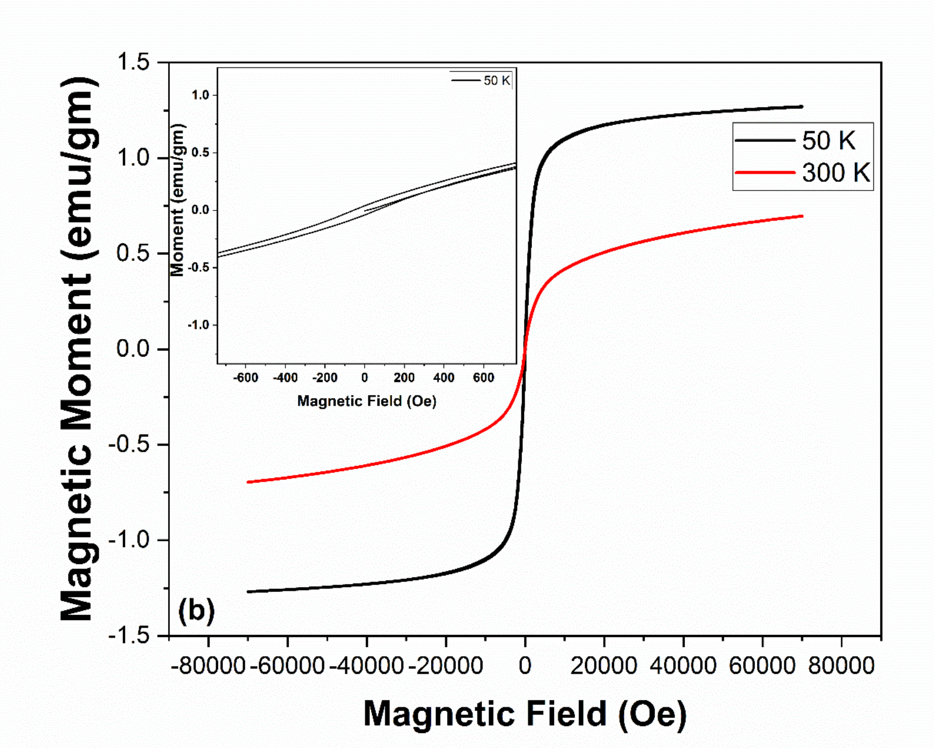

Figure 5.12(b): *M-H plot at 50K and 300K of* $Fe_{0.05}(SnTe)_{1-x}Sb_x$ *bulk alloy for x = 0.01.*

Figure 5.12(c) represents M-H curve of x = 0.03 sample and it shows a slight difference in the magnetic ordering. Along with hysteresis behaviour at lower values of magnetic field, there occurs a breaking of long-range exchange interaction that exists between the magnetic ions. This results in a spin-glass/cluster-glass state in the sample which is observed for M – H measurements at 10 K and 100 K which is due to substitution of Sb which causes a disorder in the SnTe system affecting the band structure. A co-existence of spin-glass/cluster glass-state and ferromagnetic state is observed wherein there is an enhancement in the coercivity value compared to that of x = 0 sample. No saturation is observed even in the M – H curve of 300 K, meanwhile showing hysteresis loop at lower field values. This signifies the presence of canted antiferromagnetic behaviour.

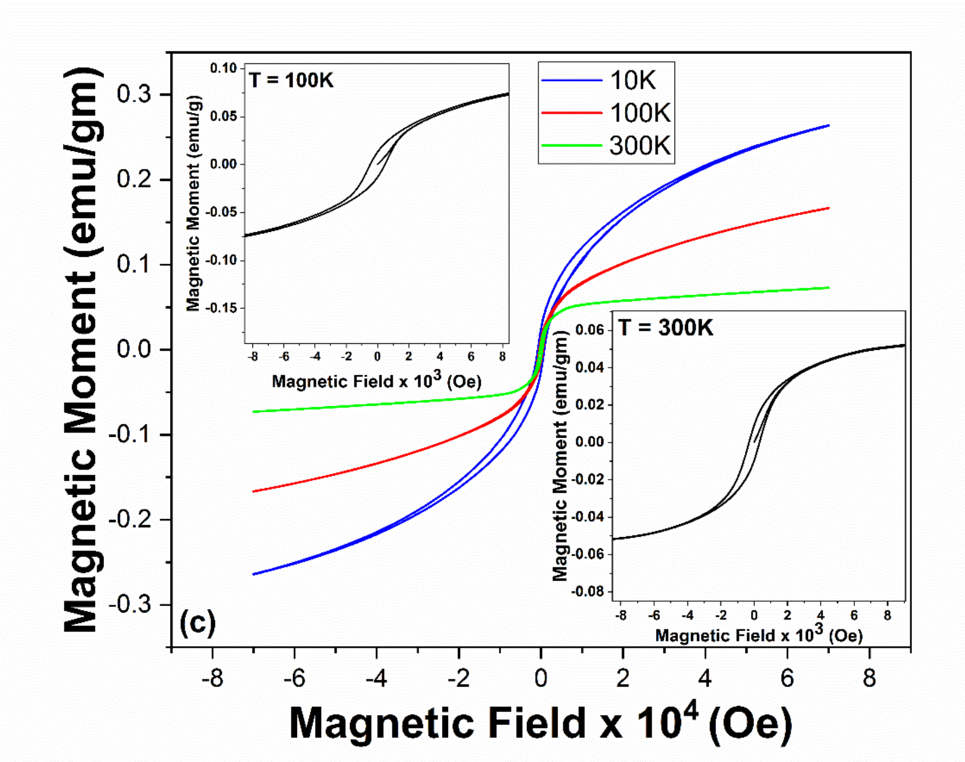

Figure 5.12(c): *M-H plot at 10K, 100K and 300K of* $Fe_{0.05}(SnTe)_{1-x}Sb_x$ *bulk alloy for x = 0.03.*

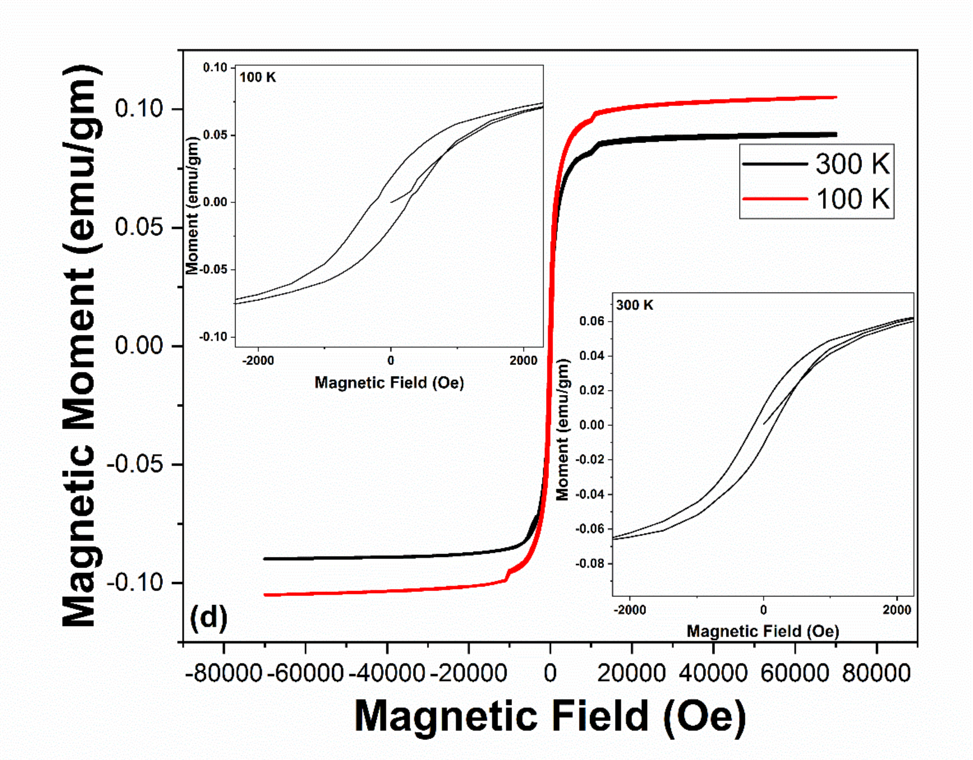

Figure 5.12(d): *M-H plot at 100K and 300K of* $Fe_{0.05}(SnTe)_{1-x}Sb_x$ *bulk alloy for x = 0.05.*

On the other hand, in x = 0.05 sample, once again the magnetization curve saturates for M – H curves measured at 100 K and 300 K and the values are ~0.11 emu/gm and ~0.09 emu/gm respectively. The plot is displayed in Fig. 5.12(d). The coercivity values of the three samples are tabulated in Table 5.7 for the purpose of comparison. They are found to decrease drastically in x = 0.05 sample compared to that of x = 0.03 sample. Doping Fe into SnTe results in magnetic ordering as observed in x = 0 sample. Substitution of Sb releases electrons into the system as it is a donor impurity. These electrons then combine with holes that are present due to Fe doping thereby undergoing compensation. This results in a suppression of ferromagnetic ordering that was brought about by holes in x = 0.01 sample. However, with increase in the concentration of Sb to x = 0.03 and 0.05, the electrons are now responsible for mediating a ferromagnetic exchange interaction between Fe ions as number of holes in the system decreases. This enhances the pinning of magnetic domains thereby bringing about an enhancement of the hysteresis response.

Table 5.7: *Comparison of coercivity values of samples measured at different temperatures.*

Samples	**Coercivity value (H_C)**			
	Oe			
	10 K	**50K**	**100 K**	**300 K**
$Fe_{0.05}(SnTe)$	133	-	-	105
$Fe_{0.05}(SnTe)_{0.99}Sb_{0.01}$	-	67	-	-
$Fe_{0.05}(SnTe)_{0.97}Sb_{0.03}$	821	-	506	318
$Fe_{0.05}(SnTe)_{0.95}Sb_{0.05}$	-	-	270	155

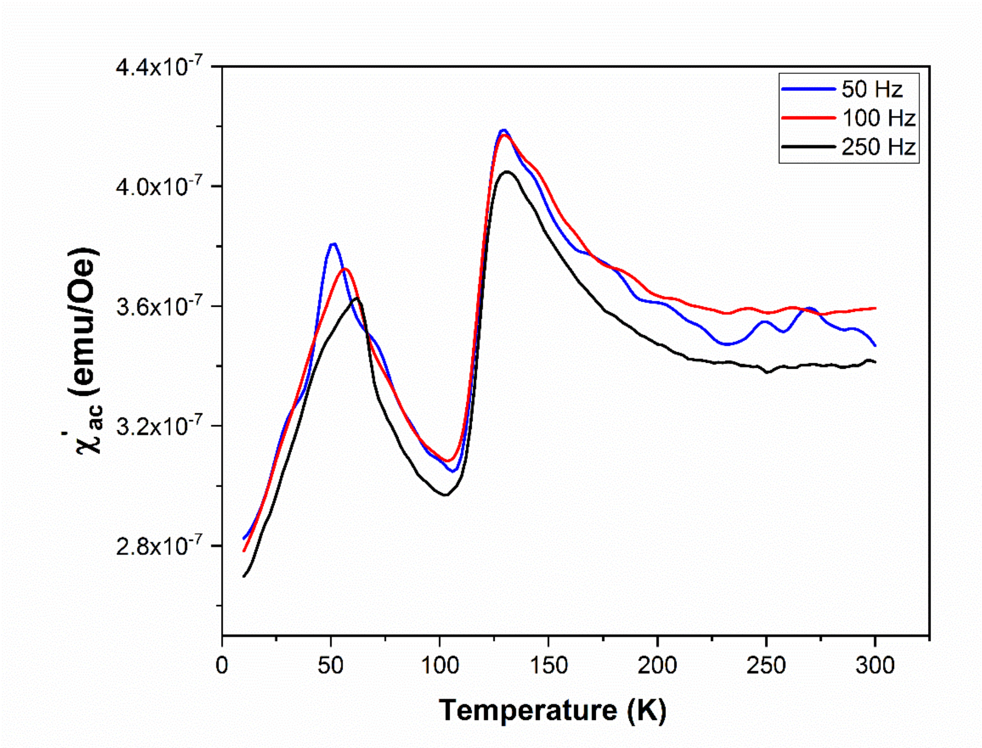

Figure 5.13: AC Susceptibility measurements at different frequencies showing the real component χ'.

From the above magnetic studies, there seems to be an appearance of a magnetic glassy state in x = 0.03 sample. Its presence can be confirmed with the help of AC susceptibility measurements performed at varying values of frequencies of 50Hz, 100Hz and 250 Hz by applying an AC field of 5 Oe. Plots of the real component of susceptibility χ' at various frequencies as a function of temperature are shown in Fig. 5.13. At a specific temperature denoted by T_m, we observe χ' to reach its maximum value. These peaks are seen to have a frequency dependence from the sizable shift of its maximum to higher values of temperature. The maximum at 51.13 K for 50 Hz displaces 62.46 K for 250 Hz and this is essentially an evidence for magnetic glassy state [50, 51]. There is another peak which is observed at all frequencies around 130 K and it can be linked to the cusp observed in Fig. 5.11(c) which shows its prominence in the DC magnetization plot of x = 0.03 sample.

The shifting of peak temperatures with frequency is better understood with the help of three empirical models that could anticipate its origins.

1. Power law $\tau = \tau^* \left(\frac{T_m}{T_g} - 1\right)^{-z\nu}$
2. Arrhenius law $\tau = \tau^* . \exp\left(\frac{E_a}{k_B . T_m}\right)$
3. Vogel – Fulcher law $\tau = \tau^* . \exp\left(\frac{E_a}{k_B . (T_m - T_0)}\right)$

$\tau = \frac{1}{2\pi f}$, T_g represents spin-glass transition temperature that corresponds to the value of T_m obtained at zero frequency, E_a is the activation energy, k_B is the Boltzmann constant.

Using the Arrhenius law, we obtain the values of parameters $\tau^* = 2.8 \times 10^{14}$ and $E_a/k_b = 546$ K [52]. The value of τ^* obtained from the Arrhenius fitting is does not lie in the range for superparamagnetic relaxation of ~ $10^{10} - 10^{13}$ s, thereby eliminating the possibility of superparamagnetic property that can also shift the values of T_m based on frequency. Figures 5.14(a) and 5.14(b) compare the plots fitted using Power law and Vogel-Fulcher law respectively.

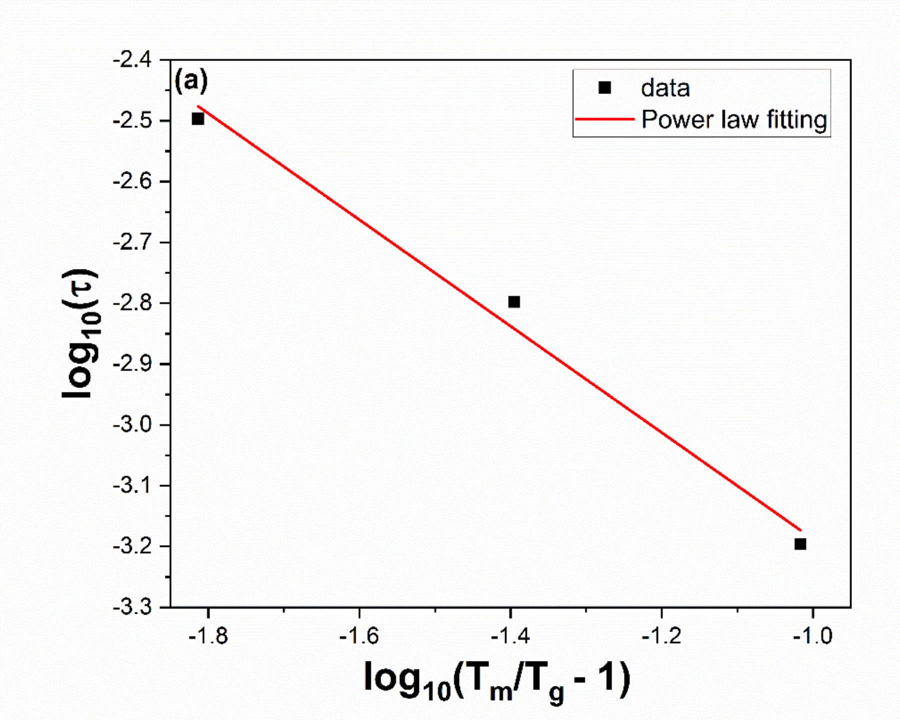

Figure 5.14(a): Data points with linear fits to Power law.

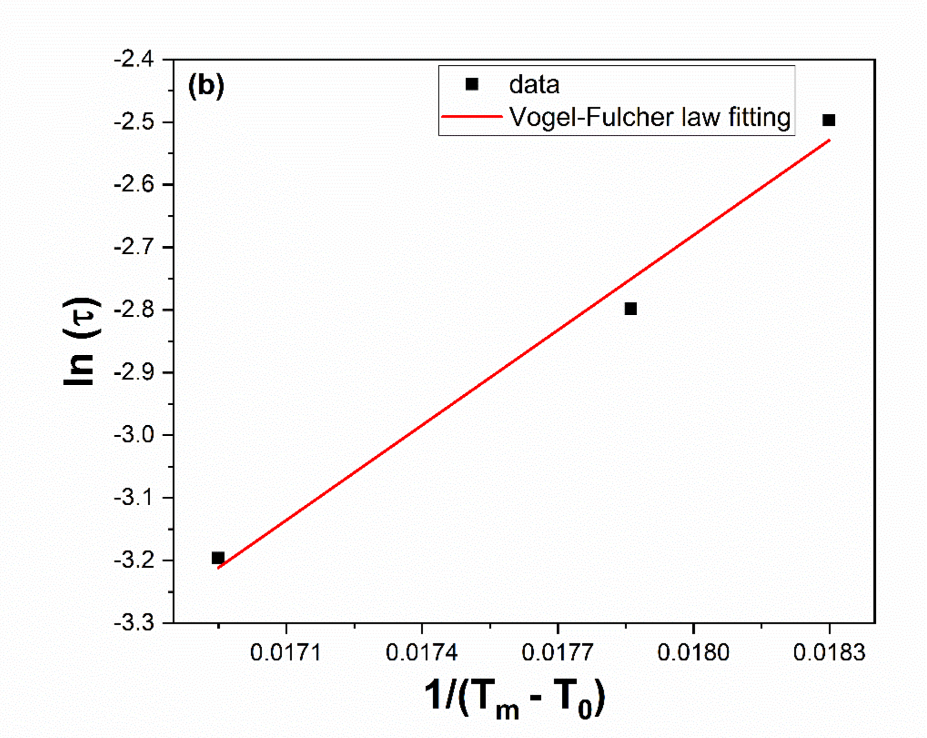

Figure 5.14(b): Data points with linear fits to Vogel-Fulcher law.

The fitted data yields $z\nu = 1.2$ and $\tau^* = 10^{-5}$ s using power law, $\tau^* = 10^{-4}$ s and $E_a/k_b = 0.29$ K using Vogel-Fulcher law [52]. The computed value of τ^* from the aforementioned models recognizes that the magnetic glassy state results from the presence of clusters of spins.

The cluster-glass feature is also confirmed by the Mydosh parameter K computed using the equation given below.

$$K = \frac{\Delta T_m}{T_m . \Delta(log_{10} f)} \tag{5.5}$$

Ideally, for a cluster-glass system, the value of K should lie between 0.005 and 0.08 [53]. For x = 0.03 sample, the value derived is 0.08. Even though cluster-glass and spin-glass are similar; however, the difference resides in the presence of the cluster of spins, which in turn gives rise to the glassy feature.

References

1. A. A. Khan, I. Khan, I. Ahmad and Z. Ali, "Thermoelectric studies of IV-VI semiconductors for renewable energy resources," Mater. Sci. Semicond. Process., vol. 48, 85 (2016).
2. P.D. Antunez, J. J. Buckley and R. L. Brutchey, "Tin and germanium monochalcogenide IV-VI semiconductor nanocrystals for use in solar cells," Nanoscale, vol. 3, 2399 (2011).
3. A. M. Mousa and J. P. Ponpon, "Optical and electrical properties of PbTe films grown by laser induced evaporation of pressed PbTe pellets," App. Surf. Sci., vol. 254, 1215 (2007).
4. R. M. Kannaujiya, A. J. Khimani, S. H. Chaki, S. M. Chauhan, A. B. Hirpara and M. P. Deshpande, "Growth and characterization of tin telluride (SnTe) single crystals," Eur. Phys. J. Plus, vol. 135, 47 (2020).
5. C. O'Neill, D. A. Sokolov, A. Hermann, A. Bossak, C. Stock and A. D. Huxley, "Inelastic x-ray investigation of the ferroelectric transition in SnTe," Phys. Rev. B Solid State, vol. 95, 144101 (2017).
6. O. Madelung, U. Rössler and M. Schulz (ed.), "Tin Telluride (SnTe) crystal structure, lattice parameters: Datasheet from Landolt-Börnstein - Group III Condensed Matter · Volume 41C: 'Non-Tetrahedrally Bonded Elements and Binary Compounds I' in SpringerMaterials (https://doi.org/10.1007/10681727_862)." Springer-Verlag Berlin Heidelberg.
7. P. B. Littlewood et al., "Band structure of SnTe studied by photoemission spectroscopy," Phys. Rev. Lett., vol. 105, 3 (2010).
8. Y. Gelbstein, "Thermoelectric power and structural properties in two-phase Sn/SnTe alloys," J. Appl. Phys., vol. 105, 10 (2009).
9. T. H. Hsieh, H. Lin, J. Liu, W. Duan, A. Bansil and L. Fu, "Topological crystalline insulators in the SnTe class materials," Nat. Commun., vol. 3, 982 (2012).

10. Y. Tanaka, Z. Ren, T. Sato, K. Nakayama, S. Souma, T. Takahashi, K. Segawa and Y. Ando, “Experimental realization of a topological crystalline insulator in SnTe,” Nat. Phys., vol. 8, 800 (2012).

11. U. S. Shenoy and D. K. Bhat, “Molybdenum as a versatile dopant in SnTe: a promising material for thermoelectric application,” Energy Adv., vol. 1, 9 (2014).

12. T. Dietl, H. Ohno, F. Matsukura, J. Cibert and D. Ferrand, “Zener Model Description of Ferromagnetism in Zinc-blende Magnetic Semiconductors,” Science, vol. 277, 1019 (2000).

13. Z. Li et al., “Surface oxidation and thermoelectric properties of indium-doped tin telluride nanowires,” Nanoscale, vol. 9, 13014 (2017).

14. D. K. Bhat and U. S. Shenoy, “Enhanced thermoelectric performance of bulk tin telluride: synergistic effect of calcium and indium co-doping,” Materials Today Physics, vol. 4, 12 (2018).

15. H. Wang et al., “Enhancement of thermoelectric performance of bulk SnTe alloys via the synergistic effect of band structure modification and chemical bond softening,” J. Mater. Chem. A, vol. 5, 14165 (2017).

16. R. M. Kannaujiya et al., “Effect of Sb doping on CVT grown SnTe single crystals electrical and thermal properties,” J Mater Sci: Mater Electron, vol. 33, 20823 (2022).

17. S. K. Gandomani, B. Khoshnevisan and R. Yousefi, “The capability of SnTe QDs as QDSCs working in the visible–NIR region and the effects of Eu-doping on improvement of solar cell parameters,” J Mater Sci: Mater Electron, vol. 29, 18989 (2018).

18. E. Salje et al., “Tin telluride: A weakly co-elastic metal,” Phys. Rev. B, vol. 82, 184112 (2010).

19. G. Balakrishnan, L. Bawden, S. Cavendish and M. R. Lees, “Superconducting properties of the In-substituted topological crystalline insulator SnTe,” Phys. Rev. B, vol. 87, 140507 (2013).

20. Y. Mizhuguchi and O. Miura, “High-pressure synthesis and superconductivity of Ag-doped topological crystalline insulator SnTe ($Sn_{1-x}Ag_xTe$ with x = 0-0.5),” J. Phys. Soc. Jpn., vol. 85, 053702 (2016).

21. M. Inoue, K. Ishii and H. Yagi, “Ferromagnetic Ordering in Mn-Doped SnTe Crystals,” J. Phys. Soc. Jpn., vol. 43, 903 (1977).

22. M. Escorne and A. Mauger, “Transport properties of $Sn_{1-x}Mn_xTe$ at low magnetic field,” J. Phys., vol. 40, 347 (1979).

23. A. J. Nadolny, J. Sadowski, B. Taliashvili et al., “Carrier induced ferromagnetism in epitaxial $Sn_{1-x}Mn_xTe$ layer,” J. Magn. Magn. Mater., vol. 248, 134 (2002).

24. K. Racka et al., “Anomalous Hall Effect in $Sn_{1-x-y}Mn_xEu_yTe$ and $Sn_{1-x-y}Mn_x Er_yTe$ Mixed Crystals,” J. Supercond. 16, 289 (2003).

25. L. Kilanski, A. Podgórni, M. Górska, W. Dobrowolski, V. E. Slynko, E. I. Slynko, A. Reszka and B. J. Kowalski, “Magnetic Properties of $Sn_{1-x}Cr_xTe$ Diluted Magnetic Semiconductors,” Acta Phys. Pol. A, vol. 124, 881 (2013).

26. M. Inoue, Y. Takai, K. Fukui, H. Yagi and T. Tatsukawa, “Magnetic properties of $Sn_{1-x}Cr_xTe$ crystals,” J. Magn. Magn. Mater., vol. 36, 255 (1983).

27. N. Wang, J. F. Wang, C. Si, B. -L. Gu and W. H. Duan, “Defect energetics and magnetic properties of 3*d*-transition-metal-doped topological crystalline insulator SnTe,” Sci. China Phys. Mech. Astron., vol. 59, 680012 (2016).

28. M. Inoue, H. Oshima, M. Morisaki, H. Yagi, H. K. Fun and T. Tatsukawa, “Various Types of Magnetism in SnTe Crystals Doped with 3d Transition Metals,” J. Phys. Soc. Japan, vol. 50, 1222 (1981).

29. S. Menon and M. Sarkar, “Optical properties and band gap tuning by co-doping of Sb in Fe doped SnTe bulk alloys,” Solid State Technology, vol. 63, 6 (2020).

30. S. K. Ghandomani, B. Khoshnevisan and R. Yousefi, “The effects of Sn:Te ratio on optical properties of SnTe NPs,” Journal of Luminescence, vol. 203, 481 (2018).

31. E. Burstein, “Anomalous optical absorption limit in InSb” Phys. Rev., vol. 93, 632 (1954).

32. T. S. Moss, “The interpretation of the properties of indium antimonide,” Proc. Phys. Soc. London, Sect. B, vol. 67, 775 (1954).

33. S. Pal et al., “Pressure-induced phase transitions in the topological crystalline insulator SnTe and its comparison with semiconducting SnSe: Raman and first-principles studies,” Phys. Rev. B. vol. 101, 155202 (2020).

34. H. Abdullah, S. A. Halim, A. N. J. Jannah, “Effect of disorder particles size of Nd on electrical transport on a bulk of $Pr_{2/3}Ba_{1/3}MnO_3$,” J. Composite Mater., vol. 46, 3103 (2012).

35. P. –H. Xiand et al., “Strain controlled metal-insulator transition in epitaxial $NdNiO_3$ thin films,” J. Appl. Phys., vol. 114, 243713 (2013).

36. Y. Xu, J. Zhang, G. Cao, C. Jing, S. Cao, “Low-temperature resistivity minimum and weak spin disorder of polycrystalline $La_{2/3}Ca_{1/3}MnO_3$ in a magnetic field,” Phys. Rev. B, vol. 73, 224410 (2006).

37. G. M. Amara, Ah. Dhahri, J. Dhahri, E. K. Hlil, “Correlation between magnetic and electric properties based on the critical behavior of resisitivity and percolation model of $La_{0.8}Ba_{0.1}Ca_{0.1}MnO_3$ polycrystalline,” RSC Adv., vol. 7, 10928 (2017).

38. X. L. Wang et al., “Giant negative magnetoresistance in Manganese-substituted Zinc Oxide,” Sci. Rep., vol. 5, 9221 (2015).

39. C. Majumder, S. Bhattacharya, T. K. Mondal and S. K. Saha, “Ferromagnetism with high magnetoresistance in Ag decorated graphitic carbon nitride,” J. Magn. Magn. Mater., vo. 535, 167941 (2021).

40. J. Hu, T. F. Rosenbaum and J. B. Betts, “Current Jets, Disorder, and Linear Magnetoresistance in the Silver Chalcogenides," Ph”s. Rev. Lett., vol. 95, 186603 (2005).

41. R. K. Willardson and J. J. Duga, “Magnetoresistance in Gallium Arsenide,” Proc. Phys. Soc., vol. 75, 280 (1960).

42. X. Wang, Y. Du, S. Dou and C. Zhang, “Room Temperature Giant and Linear Magnetoresistance in Topological Insulator Bi_2Te_3 Nanosheets,” Phys. Rev. Lett., vol. 108, 266806 (2012).

43. D. Kumar and A. Lakhani, “Large linear magnetoresistance from neutral defects in Bi_2Se_3 single crystal,” Phys. Status Solidi - Rapid Res. Lett., vol. 12, 1800088 (2018).

44. V. Saini, S. Sasmal, R. Kulkarni and A. Thamizhavel, “Linear unsaturated magnetoresistance in YSi single crystal,” Appl. Phys. Lett., vol. 119, 071904 (2021).

45. S. Menon, M. Sarkar, S. S. Nirvan and R. Venkatesh, “Transition from Metallic to Insulating Nature and Room Temperature Ferromagnetism of $Fe_{0.05}$(SnTe) Bulk Alloy,” J. Supercond. Nov. Magn., vol. 35, 1113 (2022).

46. P. J. Picone and P. E. Clark, “Mössbauer measurements on lattice and interstitial iron atoms in $Fe_{1+x}Sb$ alloys,” J. Magn. Magn. Mater., vol. 12, 233 (1979).

47. A. Saxena, P. Rani, V. Nagpal, S. Patnaik, I. Felner and V. P. S. Awana, “Crystal growth and characterization of possible new magnetic topological insulators FeBi2Te4,” J. Supercond. Nov. Magn., vol. 33, 2251 (2020).

48. K. Yadav, M. K. Sharma, S. Singh and K. Mukherjee, “Exotic magnetic behaviour and evidence of cluster glass and Griffiths like phase in Heusler alloys $Fe_{2-x}Mn_xCrAl$ ($0 \leq x \leq 1$),” Sci. Rep., vol. 9, 15888 (2019).

49. M. Kumar, R. Choudhary, D. K. Shukla and D. M. Phase, “Metastable magnetic state and magnetotransport in disordered manganite thin films,” J. Appl. Phys., vol. 115, 163904 (2014).

50. S. Mitra, O. Mondal, S. Banerjee and Dp. Chakravorty, “Observation of spin-glass behaviour in nickel adsorbed few layer graphene,” J. Appl. Phys., vol. 113, 024307 (2013).

51. Z. Fu et al., “Coexistence of magnetic order and spin-glass-like phase in the pyrochlore antiferromagnet Na3Co(CO3)2Cl,” Phys. Rev. B, vol. 87, 214406 (2013).

52. S. Menon, M. Sarkar, S. Singh and R. Venkatesh, “Magnetic glassy state in combination with ferromagnetism in $Fe_{0.05}(SnTe)_{0.97}Sb_{0.03}$ bulk alloy,” Mater. Res. Express, vol. 10, 044002 (2023).

53. P. Bag, K. Somesh and R. Nath, “A study of cluster spin-glass behaviour at the critical composition $Mn_{0.73}Fe_{0.27}NiGe$,” J. Magn. Magn. Mater., vol. 497, 165977 (2020).